

AD-A189 745

THE EFFECTIVE FRACTURE TOUGHNESS OF ALUMINUM AT RAPID
HEATING RATES(U) AIR FORCE INST OF TECH
WRIGHT-PATTERSON AFB OH SCHOOL OF ENGINEERING

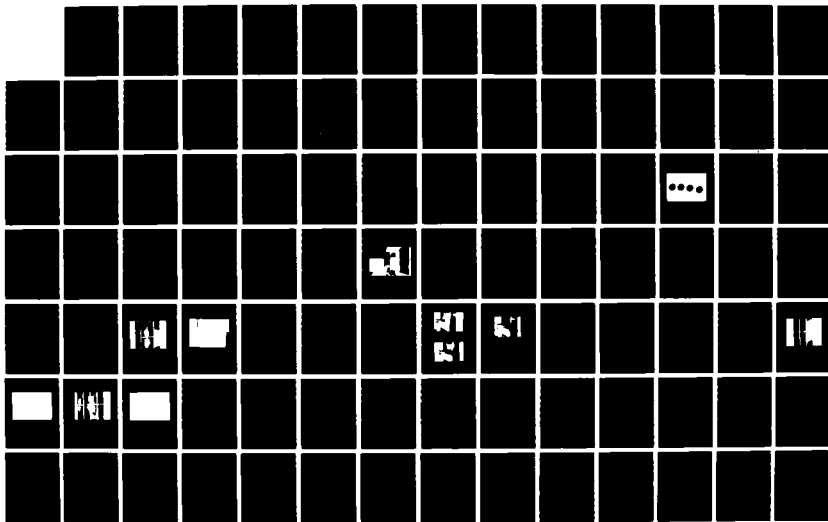
1/2

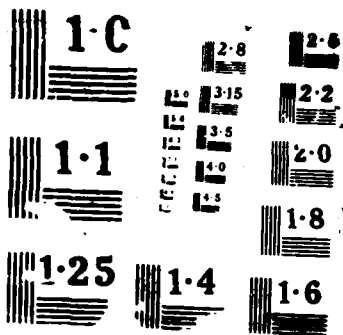
UNCLASSIFIED

J M NICHOLS DEC 87 AFIT/GAE/AA/87D-14

F/G 11/6.1

NL

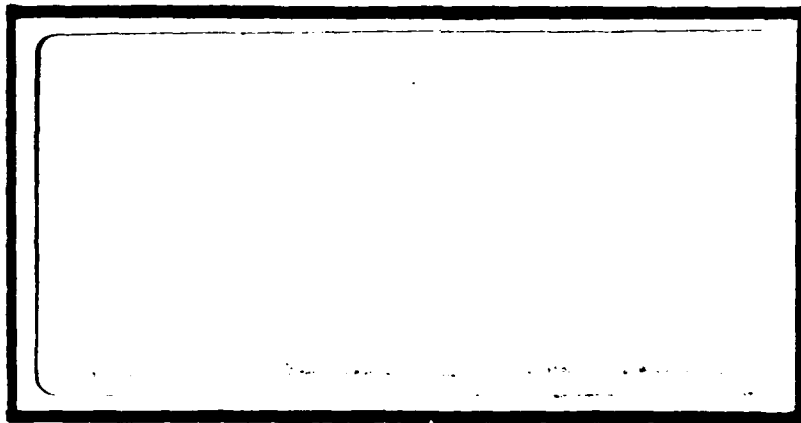




DTIC FILE COPY

1

AD-A189 745



DTIC

CTE

MAR 07 1988



∞

H



DEPARTMENT OF THE AIR FORCE
AIR UNIVERSITY

AIR FORCE INSTITUTE OF TECHNOLOGY

Wright-Patterson Air Force Base, Ohio

DISTRIBUTION STATEMENT A

Approved for public release;
Distribution Unlimited

88 3 01 061

AFIT/GAE/AA/87D-14

THE EFFECTIVE FRACTURE TOUGHNESS OF ALUMINUM
AT RAPID HEATING RATES

THESIS

Presented to the Faculty of the School of Engineering
of the Air Force Institute of Technology
Air University

In Partial Fulfillment of the
Requirements for the Degree of
Master of Science in Aeronautical Engineering

Joseph W. Nichols, B.S.
Captain, USAF

December 1987

Approved for public release; distribution unlimited

AFIT/GAE/AA/B7D-14

THE EFFECTIVE FRACTURE TOUGHNESS
OF ALUMINUM AT RAPID HEATING RATES

THESIS

Joseph W. Nichols
Captain, USAF

AFIT/GAE/AA/B7D-14

DTIC

MAR 07 1988

8 H

Approved for public release; distribution unlimited

Preface

When I was trying to decide on a thesis topic, I had hoped to find one that would allow me to combine my background in laser effects with my study in structural analysis. Thanks to my friends at the Air Force Weapons Laboratory and my faculty advisor, a topic was found that allowed me to do just that. While I am mindful of the limitations of this study, I nevertheless hope the experimental data and analysis from this thesis will provide useful information to future researchers in this area.

I wish to express my thanks to Dr Shankar Mall, my faculty advisor, for all his help in getting this thesis off the ground and seeing it through to its successful conclusion. Dr Mall's ability to quickly get to the heart of any problem was a great asset to me in doing this work. I am grateful to my former colleagues, Dr Pat Vail and Lt Col Joel Walton of the Air Force Weapons Laboratory for sponsoring this work. Dr Bill Bozich of McDonnell Douglas Astronautics gave me timely advice and assistance which was critical to the completion of this thesis; I thank him. I also wish to thank John Bagford of Accurex Corp for his untiring work in the laser laboratory and Tim Hancock of the AFIT Model Shop for his fabrication assistance. Finally, I must thank my wife, and best friend, Diane for her love and support throughout these past 18 months.

J. W. Nichols



On For	<input type="checkbox"/>
AI	<input checked="" type="checkbox"/>
ed	<input type="checkbox"/>
tion	<input type="checkbox"/>
tion/	
Availability Codes	
Available, or	
Dist	Special

A-1

Table of Contents

	Page
Preface	ii
List of Figures	v
List of Tables	vii
List of Symbols	viii
Abstract	xi
I. Introduction	1
Objectives	2
II. Background	4
Linear Elastic Fracture Mechanics	5
Temperature Effects on K_{Ic}	7
Temperature Effects on Strength	7
Fracture Mechanics of Ductile Materials	10
Laser Interactions with Metals	12
Laser Interactions with Pressurized Shells	15
Previous Laser Interaction Fracture Tests	17
III. Experimental Procedure	18
Specimen Preparation	18
High Temperature Tests	22
Room Temperature Tests	37
Uncertainty Analysis	37
IV. Results and Discussion	40
Tensile Tests	40
Fracture Tests	43
Ductile Failure Analysis	61
V. Conclusions	66
Appendix A: Thermal Coupling and Through-Thickness Temperature Calculations	68
Appendix B: Calculation Procedure for Computing the Critical Crack Length using Ductile Fracture Mechanics	71

Appendix C: Critical Crack Length Calculations using Ductile Fracture Mechanics	77
Appendix D: Data Tables	79
Bibliography	85
Uita	87

List of Figures

Figure	Page
1. The Three Modes of Loading	5
2. Effect of Temperature on the Ultimate Strength of 6061 T-6 Aluminum Alloy	9
3. Room Temperature Absorptance Versus Wavelength for Various Materials	14
4. MDAC-LMSC Model for Predicting Rupture in Pressurized 6061 T-6 Aluminum Cylinders	16
5. Specimen Design and Labeling Scheme	19
6. Specimen Instrumentation	23
7. LHMEI Test Cell Lay-out	24
8. Plexiglas Beam Impressions	25
9. Typical Temperature Versus Time Relation at Center of Plate	30
10. Stress Versus Time Relation During Test Under Hydraulic (Tinius-Olsen) Loading Device	32
11. Creep Rupture Tester (SAITEC) Drawing	33
12. SEN Specimen in Tensile Grips	34
13. Load Versus Time Histories for each Heating Rate	36
14. Room Temperature Stress-Strain Curves for 6061 T-6 Aluminum used in Fracture Tests	38
15. Effect of Temperature on the Ultimate Strength of 6061 T-6 Aluminum	42
16. 6061 T-6 Aluminum Tensile Specimen-- After Tensile Tests	44
17. 6061 T-6 Aluminum Tensile Specimen--Fracture Surfaces After Tensile Tests	45
18. Room Temperature Failure Loads Versus Crack Length of SEN, .061 in thick, 1.5 in wide 6061 T-6 Aluminum	47
19. Crack Propagation Sequence in Specimen A-27	49

20.	Crack Propagation Sequence in Specimen A-27 . . .	49
21.	Crack Propagation Sequence in Specimen A-27 . . .	50
22.	K_C^* Versus Temperature Relation for 6061 T-6 Aluminum (.033 in thick)	51
23.	K_C^* Versus Temperature Relation for 6061 T-6 Aluminum (.061 in thick)	52
24.	Normalized K_C^* Versus Temperature Relation for 6061 T-6 Aluminum	54
25.	Single Edge Notched Specimen-- After Fracture Tests	55
26.	SEN Fracture Surfaces--After Fracture Tests . . .	56
27.	SEN and CCP Specimen--After Fracture Tests. . .	57
28.	SEN and CCP Fracture Surfaces After Fracture Tests	58
29.	Limit Load Versus Temperature Relation along with Measured Failure Loads For SEN, 0.061 inch thick, 1.5 inch wide 6061 T-6 Aluminum, with crack length = .367 in	59
30.	Stress-Strain Curves for 6061 T-6 Aluminum Under Rapid Heating	62
31.	Comparison of Measured Fracture Strength of 6061 T-6 Aluminum with Ductile Fracture Model at 150°C	63
32.	Comparison of Measured Fracture Strength of 6061 T-6 Aluminum with Ductile Fracture Model at 370°C	64
33.	Relationship Between w_f and w_u for Different Stress-Strain Curves	73

List of Tables

Table	Page
I. Experimental Apparatus	20
II. Fatigue Pre-Cracking Details	21
III. Heating Rate Designations	26
IV. Average Surface Absorptivities for 6061 T-6 Aluminum at 10.6 μm	28
V. Strength Properties of 6061 T-6 Aluminum	41
VI. Room Temperature Fracture Toughness for 6061 T-6 Aluminum (1.5 in Width)	43
C.1. Critical Crack Length Versus Stress Using Ductile Fracture Mechanics at 150 C	77
C.2. Critical Crack Length Versus Stress Using Ductile Fracture Mechanics at 370 C	78
D.1. Room Temperature Tensile Tests of 6061 T-6 Aluminum (.061 in thick)	79
D.2. Room Temperature Tensile Tests of 6061 T-6 Aluminum (.033 in thick)	80
D.3. Rapid Heating Tensile Tests of 6061 T-6 Aluminum (1.5 in wide, .061 in thick)	80
D.4. Room Temperature Fracture Toughness (K_{IC}^*) and Net Section Limit Loads (P_1, P_u) for 6061 T-6 Aluminum (.061 in thick)	81
D.5. Room Temperature Fracture Toughness (K_{IC}^*) and Net Section Limit Loads (P_1, P_u) for 6061 T-6 Aluminum (.033 in thick)	82
D.6. Rapid Heating Rate Fracture Toughness (K_{IC}^*) and Net Section Limit load (P_1) for 6061 T-6 Aluminum (1.5 in wide, .061 in thick)	83
D.7. Rapid Heating Rate Fracture Toughness (K_{IC}^*) and Net Section Limit Load (P_1) for 6061 T-6 Aluminum (1.5 in wide, .033 in thick)	84

List of Symbols

A	Nominal cross-sectional (in), laser spot area (cm)
a	Crack length (in)
B	thickness (in)
b	$W - a$
C_p	Specific heat (J/g°K)
E	Young's modulus (psi)
G_c	Crack driving force
h	Effective height of slip band
I	Incident energy density--intensity (kW/cm ²)
k	Thermal conductivity (W/cm°K)
K	Stress intensity factor
K_{Ic}	Plane strain fracture toughness (ksi $\sqrt{\text{in}}$)
K_{Ic}^*	$K_{Ic}(T, \dot{T})$
L_f	Failure Load (lb)
L_i	Initial Load (lb)
L_y	Load at Yield (lb)
l	Plate thickness
N	Number of Fatigue Cycles
n	Ramberg-Osgood exponent for true plastic tensile strain
P	Laser power on the specimen
P_l	Net section limit load for elastic-perfectly plastic material
P_u	Net section limit load using ultimate strength
q	Absorbed energy density (kW/cm ²)
T	Temperature (°C), energy required to break atomic bonds
T_f	Failure temperature (°C)

T_m	Melt temperature
T_i	Initial temperature
t	Time (sec)
U_e	Strain energy available to create new crack surfaces
U_p	Plastic strain energy
U_s	Strain energy consumed in creating new crack surfaces
W	Specimen width (in)
W_f	Unrecoverable energy under stress-strain curve from applied stress to ultimate stress
W_u	Strain energy under stress-strain curve from ultimate stress to failure stress
x	Distance through thickness of plate (cm)
α	Absorptivity
β	Geometric correction for finite width plate
ϵ	Uniaxial tensile strain
ϵ_{pn}	Corrected plastic tensile strain
ϵ_t	True tensile strain
ϵ_{tf}	True Tensile strain at failure
ϵ_{tu}	True Tensile strain at ultimate stress
ϵ_{tpu}	True Tensile strain at start of necking
μ	Thickness parameter
ν	Poisson's ratio
κ	Thermal diffusivity
ϕ	Thickness Parameter
ρ	Density
σ	Uniaxial tensile stress
σ_y	Yield stress
σ_u	Ultimate stress

σ_f Failure stress

σ_{uf} Average uniaxial tensile stress from 0.995 q_u to q_f

σ_{tu} True ultimate tensile stress

σ_{tf} True tensile stress at failure

σ_{ty} True tensile stress at yield

σ_{tl} Arbitrary elastic limit tensile stress
at plastic strain = 0.0005

Abstract

The fracture of aluminum plates, at high temperatures and at rapid heating rates, was investigated using 6061 T-6 aluminum as the test material. Three heating rates were tried--low (15°C/sec), medium (150°C/sec), and high (1500°C/sec).

Rapid heating and room temperature tensile tests were performed to characterize the material as a function of temperature. Single edge notched specimen and center cracked panels were fabricated for use in fracture tests. A modified linear elastic fracture toughness, called the effective fracture toughness, or K_C^* was used to quantify the relationship between fracture toughness and temperature. The K_C^* was found to decrease as temperature increased in the same manner as the strength. Heating rate, at least in the range tested, had little effect on either the strength or the fracture toughness. Further, it was found that the fracture behavior of 6061 T-6 aluminum under the tested conditions can be related to net-section yielding.

A ductile fracture model was found to be useful in relating the critical crack size to critical stress. The test data from the present study showed good agreement with this model.

I. Introduction

On September 6, 1985 at the White Sands Missile Range, a large booster rocket stage was destroyed by laser radiation. Aviation Week and Space Technology reported that a Titan I second stage, pressurized to simulate flight loads, exploded after being irradiated by a Navy laser in the first lethality test for the Strategic Defense Initiative (9:17). The New York Times reported it this way:

"It's a dramatic picture," he [Lt Gen Abrahamson] said. "When you see this large section of this booster and then you're looking at it, and they say, 'the laser's on target,' and then it just goes ... it shatters all over the place. Very, very dramatic." (16)

The test illustrated how a laser might be used in the future as a weapon. It also showed that the failure of pressurized metal structures due to rapid, localized heating may well become an important design consideration for future missiles and aircraft.

The analysis of high temperature fracture mechanics in aluminum is a relatively new problem. It is one that is complicated by the variation in many of the material properties with temperature; not just the resistance to cracking or fracture toughness. At room temperature the fracture toughness of most aerospace materials is well known. However, fracture mechanics data for higher temperatures is hard to find and data as a function of heating rate is non-existent.

Nevertheless, the failure of a pressurized cylinder due to localized laser radiation has been researched in some detail. It has been found that cylinders fail in two ways--by catastrophic rupture, or by melting a hole in the wall of the cylinder (6). Rupture occurs at temperatures well below the melting point of the metal. This is an important topic in lethality and survivability; because by creating the proper conditions for rupture, rather than melting, a minimum amount of laser energy is used to destroy the target. Many of the models used in these analyses are based upon empirical relationships between laser spot size and the geometry of the cylinder. As a result, there is little data available which relates critical crack size to the stress at failure for rapid heating.

While laser interaction with pressurized cylinders was the motivation behind this study, to simplify the problem, a flat plate in uniaxial tension was the chosen structure for investigation. A flat plate should be a good first order representation of pressurized structures with large diameters; however, it will be left to others to verify this. It is the intent of this thesis to acquire basic fracture data at high temperatures and rapid heating rates and then apply fracture mechanics principles in order to analyze it.

Objectives

The main objective of this research was to quantify the influence of temperature and heating rate on the fracture

toughness of aluminum. In order to do this the secondary objectives were:

1. Design and fabricate tensile and fracture specimen for use in laser interactions tests--considering laser power and spot size.

2. While under a uniaxial tensile load, irradiate the specimen at various intensities to induce several heating rates.

3. Measure the temperature, load, and crack length during irradiation.

4. Collect the data and analyse it using fracture mechanics.

II. Background

It is almost impossible to write anything on fracture mechanics without at least mentioning the founding fathers of the field--A. A. Griffith and G. R. Irwin (14:4). Griffith's (S:4; 7:23) main contribution, in the early 1920s, was to establish a relationship between strength and crack size based upon the amount of energy required to create new crack surfaces. The critical condition for a through-the-thickness crack to propagate can be stated mathematically as

$$\frac{\partial}{\partial a}(U_e - U_s) = 0 \quad (1)$$

where

- a = half crack length for center crack panel
- U_e = the energy consumed per unit thickness in creating the new crack surfaces. $U_s = 4aI$, where I is the work done in breaking atomic bonds.
- U_s = the energy per unit thickness available to create the new crack surfaces resulting from a crack of length $2a$ in a thin plate of infinite size under a tensile stress, σ , normal to the plane of the crack.

$$U_e = \frac{\pi \sigma^2 a^2}{E}$$

and for the half crack length

$$\frac{\partial U_e}{\partial a} = \frac{\pi \sigma^2 a}{E} = G_c \quad (2)$$

where

- σ = normal stress
- E = Young's Modulus
- G_c = the crack driving force (material constant for small plasticity near the crack)

The modern engineering discipline of fracture mechanics was born in the late 1940s when George Irwin developed the basics of linear elastic fracture mechanics. He expanded upon the work of Griffith and introduced the concept of fracture toughness (14:4). This chapter will summarize some of the principal works that have formed the basis for this thesis. While an effort has been made to address the relevant features of the previous fracture studies, this is not an exhaustive survey.

Linear Elastic Fracture Mechanics (LEFM)

A crack in a solid can be stressed in three different directions as can be seen in Figure 1. Mode I is caused by normal stresses which tend to open or separate the crack surfaces. Mode II results from "in plane shear" and is sometimes referred to as the "sliding mode." Mode III, or the "tearing mode", is caused by shear stresses out of plane (7:8,9). The principal stresses considered in this thesis are normal to the crack face and, therefore, all of the cracks studied will be of the mode I type.

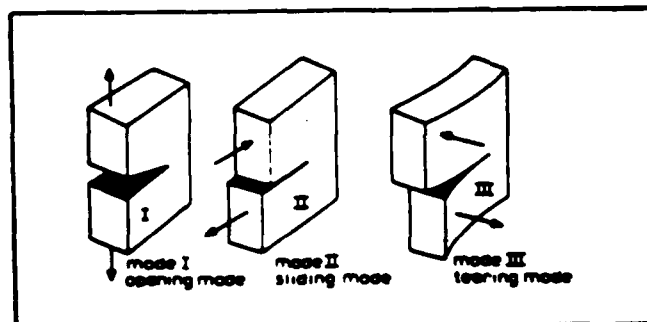


Figure 1. The Three Modes of Loading (7:8)

It was Irwin (19:49,50) who discovered that the local stresses near a crack depend upon the nominal stresses, σ , and the square root of the crack length, a . This lead to the forming of a similitude parameter called the stress intensity factor, K . For an infinitely sharp elastic crack in a wide plate:

$$K = \sigma \sqrt{\pi a} \quad (3)$$

For a given crack size, the stress intensity factor can be used to predict the stress at which fracture will occur. Therefore, when $\sigma = \sigma_c$ the stress intensity factor is known as the fracture toughness K_c ; in other words the resistance of a material to cracking. K_c is related to equation (2) in the Griffith theory through the Irwin-Orowan (5:5) relation

$$G_c = \frac{K_c^2}{E} \quad (4)$$

This shows that the stress criterion and the energy criterion are solved simultaneously (7:24).

While the K_c is not a material property, it approaches a constant value for thick plates ($B > 2.5(K_c/\sigma_y)^2$); this is the plane strain condition. In plane strain, the amount of plastic deformation near the crack tip is small enough to be neglected. For plates with thickness equal to or larger than the critical thickness for the plane strain condition the fracture toughness is assumed to be constant. However, for thinner plates, in the plane stress or transitional condition, K_c does vary with plate thickness. For many aerospace structures, the thickness is considerably less than

that required for plane strain. In this thesis the aluminum plate thicknesses are roughly in the plane stress condition at room temperature. Therefore, when K_{IC} is mentioned in this thesis or any of the other parameters derived from it, it will be understood to be a function of plate thickness.

Temperature Effects on K_{IC}

Much of the early research into the effect of temperature on the fracture toughness centered around cryogenic temperatures (23:69-107). Many metals become very brittle at low temperatures and the fracture toughness drops dramatically near what is called the nil ductility temperature (NDT). The NDT is the point where the yield strength and ultimate strength are the same. Many metals show increased fracture toughness as temperature increases. In aluminum, fracture toughness decreases from a temperature of -320°F to room temperature. The reason for this can be traced to an unusual relationship between ultimate and yield strength--the difference between the two actually diverges at low temperatures. While these results do not say much about how the fracture toughness will behave at elevated temperatures, it does illustrate how the variation of strength with temperature plays a significant role in determining the fracture toughness.

Temperature Effects on Strength

To begin with, it is apparent from Figure 2 that as temperature increases, the strength decreases. However, this

phenomenon is more complex than just that observation. At elevated temperatures, creep is responsible for not only a temperature relationship with strength, but a heating rate relationship as well.

Creep can be roughly divided into two categories--low and high temperature creep. Low temperature creep occurs at temperatures below $0.5 T_m$ (melting temperature). The major mechanism for low temperature creep in aluminum is cross-slip. This occurs when the micro-grains of the material slip past each other. High temperature creep occurs at temperatures above $0.5 T_m$ and is characterized by diffusion of alloy elements or impurities into the atomic lattice structure (12:77,81,102).

Whatever the mechanism, it is apparent from Figure 2, that the amount of time the metal spends at a given temperature has an effect on the strength. It seems that the quicker a material is heated, the less time the creep mechanisms have to work, and therefore, the strength is higher for shorter soak times. MIL Handbook (8:3-229) includes data for 10,000 hr temperature soak to 1/2 hr soak. For laser interactions, failure typically occurs much quicker than this--from several seconds to fractions of a second. Lockheed Missiles and Space Company (LMSC) measured the strength of 6061 T-6 aluminum for 8 second heating time (10:23). These results are also shown in Figure 2. It can be readily observed that the trend for the 8 second heating time data remains the same as for the MIL Handbook data.

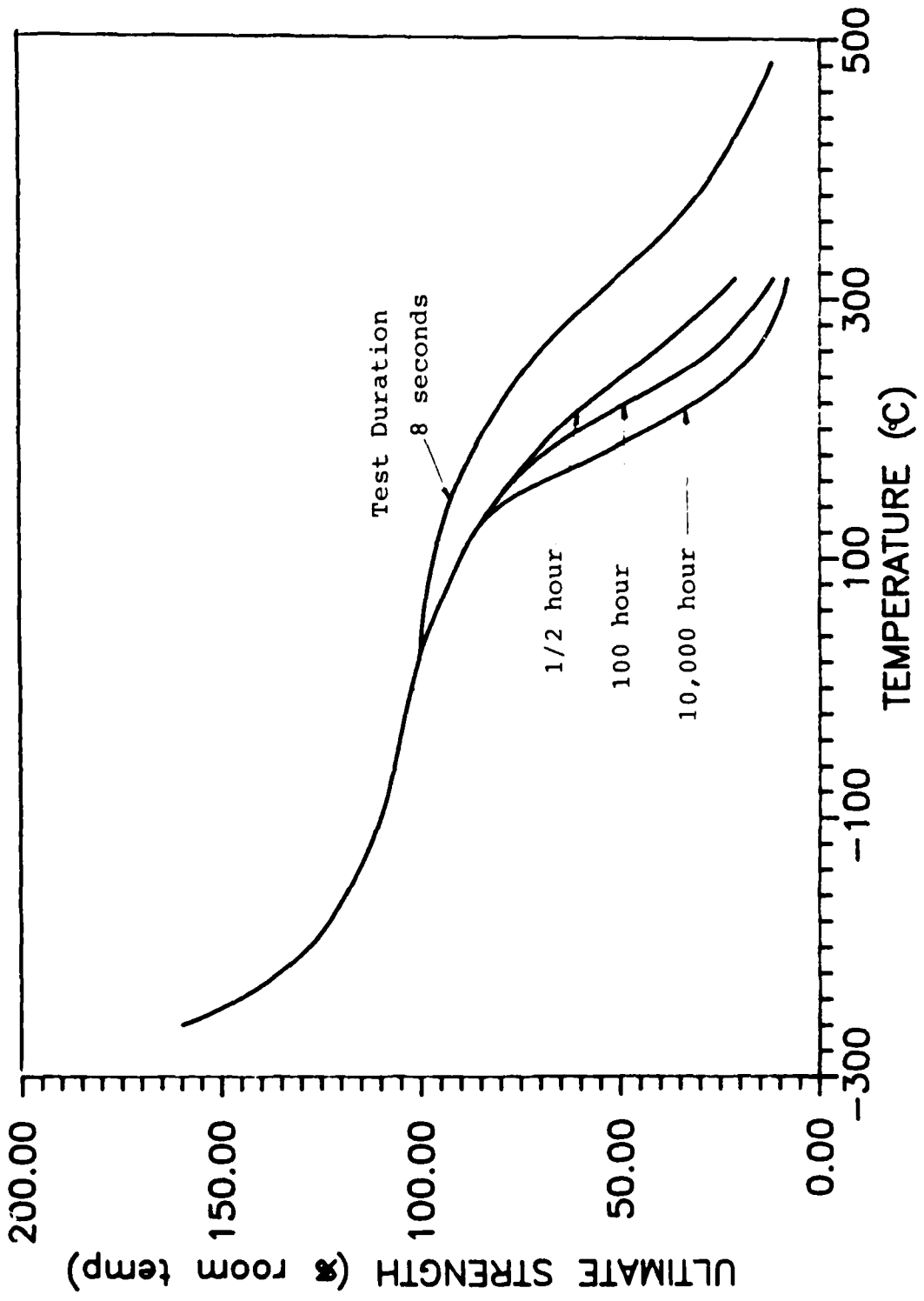


Figure 2. Effect of Temperature on the Ultimate Tensile Strength of 6061 T-6 Aluminum Alloy (8:3-229; 10:23)

The strength of aluminum has been shown to be a function of both temperature and heating rate. Therefore, recalling the definition of fracture toughness from equation (3), a modified K_C , hereafter denoted by K_C^* , is defined:

$$K_C^* = \sigma_c \sqrt{a} \beta \quad (5)$$

where

- K_C^* = $K(I, \dot{I})$
- a = initial crack length
- σ_c = failure stress
- β = specimen geometric factor

Fracture Mechanics of Ductile Materials

Almost all metals exhibit some plastic deformation near the crack tip before catastrophic crack propagation (5:5).

If this plastic deformation is small, the linear-elastic K_C^* , or K_C^* , is an appropriate way to represent the fracture toughness. As the ductility of the material increases, the amount of plastic deformation increases. Recalling equation (1) which states the basic theory developed by Griffith (5:10) and expanding it to include the energy consumed in plastic straining at the crack tip, U_p , the failure criterion becomes

$$\frac{\partial}{\partial a}(U_e - U_s - U_p) = 0 \quad (6)$$

Bockrath and Glassco (5) developed this relation into an equation which relates the critical crack size to the stress. From linear elastic theory, the elastic energy release rate is

$$\frac{\partial U_e}{\partial a} = \frac{\pi \sigma_u^2 a}{E} \quad (2)$$

and also from LEFM, the energy required to create new crack surfaces is

$$\frac{\partial U_s}{\partial a} = 2I \quad (7)$$

and finally, the plastic strain energy rate is defined as

$$\frac{\partial U_p}{\partial a} = W_f h + W_u h \quad (8)$$

where

- W_f - the plastic strain energy absorption rate above the ultimate stress at the crack tip.
- W_u - the plastic strain energy absorption rate below the ultimate stress in the region surrounding the crack tip.
- h - height of strained region at crack tip.

The W_f is determined based on the amount of energy absorbed by the slip band at the crack tip. While W_u is the unrecoverable energy under the uniaxial stress-strain curve from σ to σ_u . These two quantities can be determined from the material stress-strain curve. The method by which the following equations are derived from the stress-strain curve is outlined in Appedix B.

For plane stress

$$W_f h = \sigma_{uf} \epsilon_{pn} h_f \quad (9)$$

where

- σ_{uf} - average tensile stress from 0.995 σ_u to σ_f .
- ϵ_{pn} - difference in true tensile strain at fracture and at the start of necking.
- h_f - effective height of strained region at crack tip

For a finite width plate

$$W_{uh} = \frac{n}{n+1} \frac{\epsilon_{tpu} \sigma_{tu}}{Y^6} \left[1 - \left(\frac{\sigma_t}{\sigma_{tu}} \right)^{n+1} \right] h_f \frac{\epsilon_{tf} \epsilon_{tl}}{\epsilon_{tu} \epsilon_t} \left[\left(\frac{\epsilon_{tu}}{\epsilon_t} \right)^{\frac{n-1}{n}} - 1 \right] \phi \quad (10)$$

where

- n = the Ramberg-Osgood exponent for true plastic tensile strain
- σ_{tpu} = true plastic tensile strain at start of necking
- σ_{tu} = true ultimate tensile stress
- Y = geometric correction factor
- σ_t = true tensile stress
- h_f = effective height of slip band, .000557 in
- ϵ_{tf} = true tensile strain at $\sigma = \sigma_f$
- ϵ_{tu} = true tensile strain at start of necking
- ϵ_{tl} = true tensile strain at $\sigma = \sigma_l$
- ϵ_t = true tensile strain
- ϕ = thickness parameter ($\phi = 1.3$ for plane stress)

Substituting (2) (7) (9) and (10) into (6) yields the equation for critical crack length as a function of stress and material properties:

$$a = \frac{E}{\pi \sigma^2 Y^2} (2T + \sigma_{uf} \epsilon_{pn} h_f + \quad (11)$$

$$\frac{n}{n-1} \frac{\epsilon_{tpu} \sigma_{tu}}{Y^6} \left[1 - \left(\frac{\sigma_t}{\sigma_{tu}} \right)^{n+1} \right] h \frac{\epsilon_{tf} \epsilon_{tl}}{\epsilon_{tu} \epsilon_t} \left[\left(\frac{\epsilon_{tu}}{\epsilon_t} \right)^{\frac{n-1}{n}} - 1 \right] \phi)$$

Laser Interactions with Metals

For continuous wave lasers operating in the optical spectrum the deposition of energy into the metal is a surface phenomenon which is governed by the surface conditions of the metal and the wavelength of the radiation. The dimensionless parameter α is called the coupling coefficient and is the fraction of incident radiation absorbed by the metal. The energy density absorbed by the plate, q , is therefore

$$q = I \alpha \quad (12)$$

where

I = incident intensity (kW/cm^2)

Figure 3 is a graph of the coupling coefficients for several metals as a function of wavelength. The laser wavelength used in this experiment is $10.6 \mu\text{m}$. Once the intensity and coupling are known, the problem becomes a heat conduction problem (21:1)--for most applications, convective and radiative terms are negligible.

For intensities high enough to cause surface vaporization or plasma ignition, pressure waves can cause significant stresses in the metal (19:121-123). The present study is far removed from any of these effects. However, thermal stresses can also be significant at lower intensities when the differences in thermal expansion between the heated and non-heated areas becomes large or there is a large temperature gradient through the thickness of the metal (19). These effects were minimized in the present study by the fact that: the specimen were very thin and the temperature through the thickness was shown to be essentially constant, and the specimen were flood loaded--beam spilling over both sides of the specimen--so that the thermal expansion was directed along the line of the applied load. In short, thermal stresses were not expected to be significant in this study.

The next subsection deals with the fracture of aluminum shells when directly heated by laser radiation.

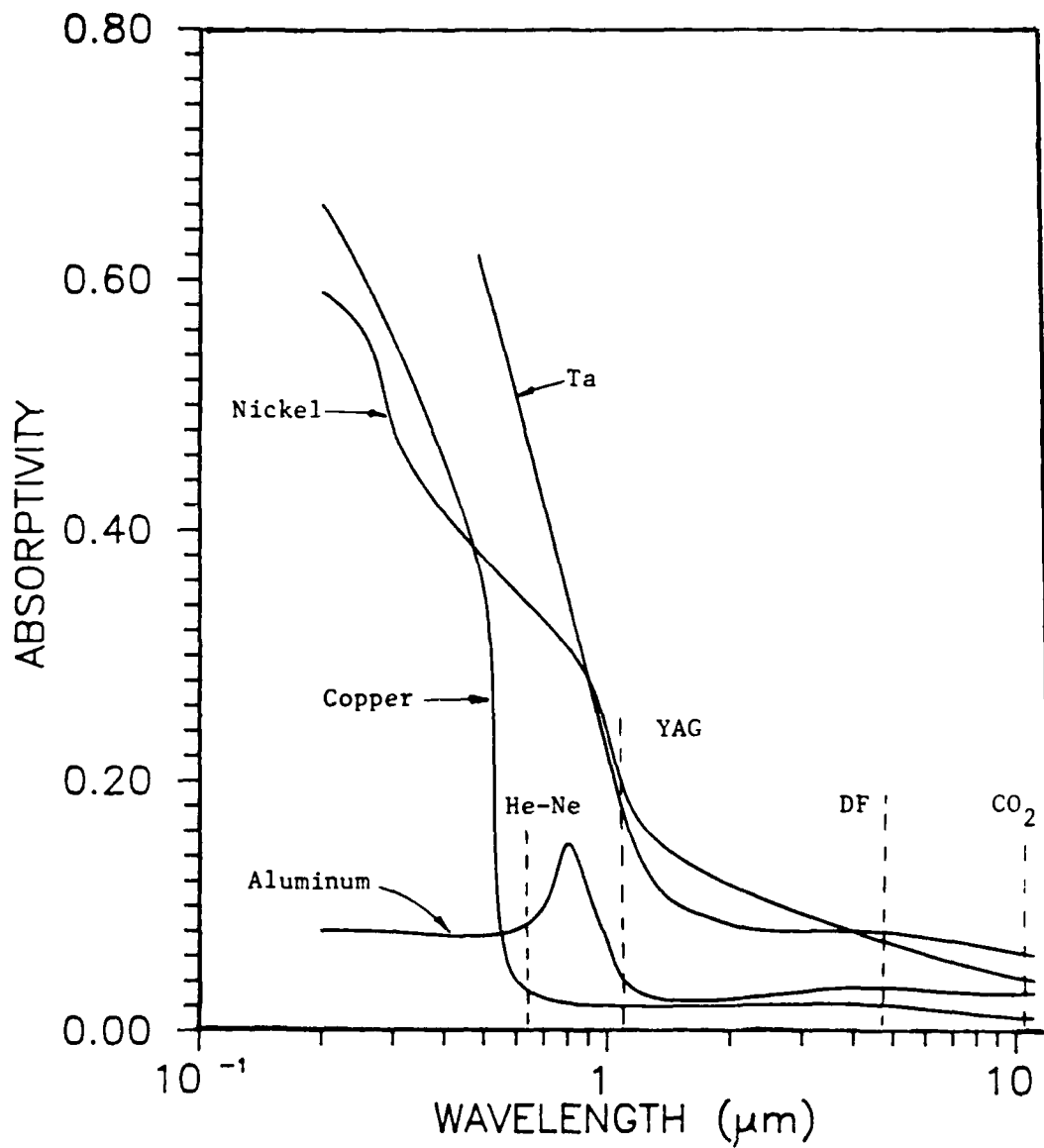


Figure 3. Room Temperature Absorptance Versus Wavelength for Various Materials

Laser Interactions with Pressurized Shells

One of the first attempt to develop a model for the rupture of pressurized cylinders through laser interaction was made by McDonnell Douglas Astronautics Corporation (MDAC) and LMSC under a contract from the Air Force Weapons Laboratory (6). Early experiments showed that when the laser heated the pressurized metal cylinder, a bulge was created by the thermal expansion in the heated zone. The failure model used the temperature dependant strength properties of aluminum along with a three-dimensional Von-Mises criteria to predict crack initiation. Crack propagation was predicted using an empirical model which related the stress in the cylinder to the the ratio of laser spot size divided by the diameter of the cylinder. This model assumes that the laser beam intensity is high enough to induce one-dimensional heat transfer. Figure 4 shows the crack propagation model for 6061 T-6 aluminum. The demarcation between burst and crack arrest was determined experimentally by irradiating cylinders with different internal pressures with laser beams of different sizes to induce rupture or depressurization (crack arrest). This model worked well for tank sizes between 1 and 2 feet in diameter. However, when this model was applied to tanks of larger diameters, some inconsistencies were found.

Other models have been suggested which are variations on the MDAC-LMSC model. However, none of these models rely on an independent validation of the critical crack length or directly consider the variation of K_c with temperature. So,

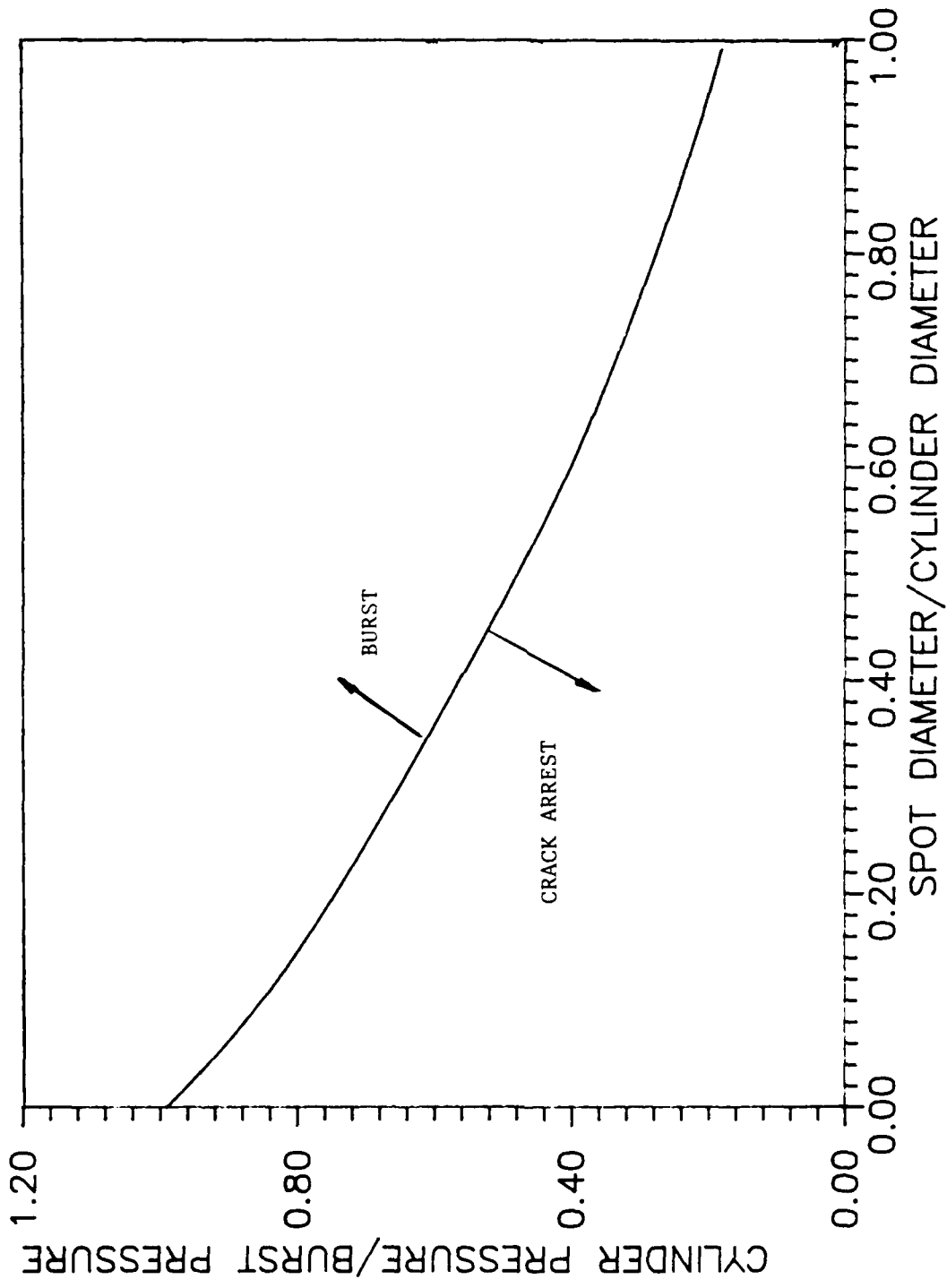


Figure 4. MDAC-LMSC (6) Model for Predicting Rupture in Pressurized 6061 Aluminum Cylinders

while these models are useful in their realm--predicting rupture of pressurized shells, they are little help in determining the basic fracture toughness of the material as a function of temperature.

Previous Laser Interaction Fracture Tests

At least one attempt was made to determine the fracture toughness of aluminum through laser interactions. The Army Materials Technology Laboratory (2) used the same laser that was used in this thesis to damage aluminum plates and torsion tubes after which the materials were stressed to failure. This work produced data on the residual strength of damaged structures, but because of the inability of the load fixture to respond to rapid thermal expansion (a problem encountered early in this work), fracture data as a function of temperature could not be obtained.

III. Experimental Procedure

The laser interaction portion of this thesis was carried out in three test series approximately one month apart. They were conducted at the Laser Hardened Materials Environmental Laboratory (LHMEL) which is located in building 71A on Wright-Patterson AFB. In addition to the high temperature work, a number of tensile and fracture tests were conducted at room temperature in Room 150 of the AFIT Engineering Building. This chapter will discuss the major apparatus and the methodology used to take the data.

Table I is a summary of the major pieces of equipment that were used in the experiments.

Specimen Preparation

Since strength data for 6061 T-6 aluminum at rapid heating rates are available, it was chosen as the test material in the present investigation. Both 0.061 and 0.033 inch thick aluminum sheet was used to make specimen. The samples were cut with the long dimension in the direction of the rolling and the crack running transverse to the rolling (ie. L-T specimen). Two types of fracture specimen were used--single edge notched (SEN) and center cracked panels (CCP). The starter notches were electric discharge machined (EDM). Figure 5 is a schematic of the specimen configurations and labeling scheme.

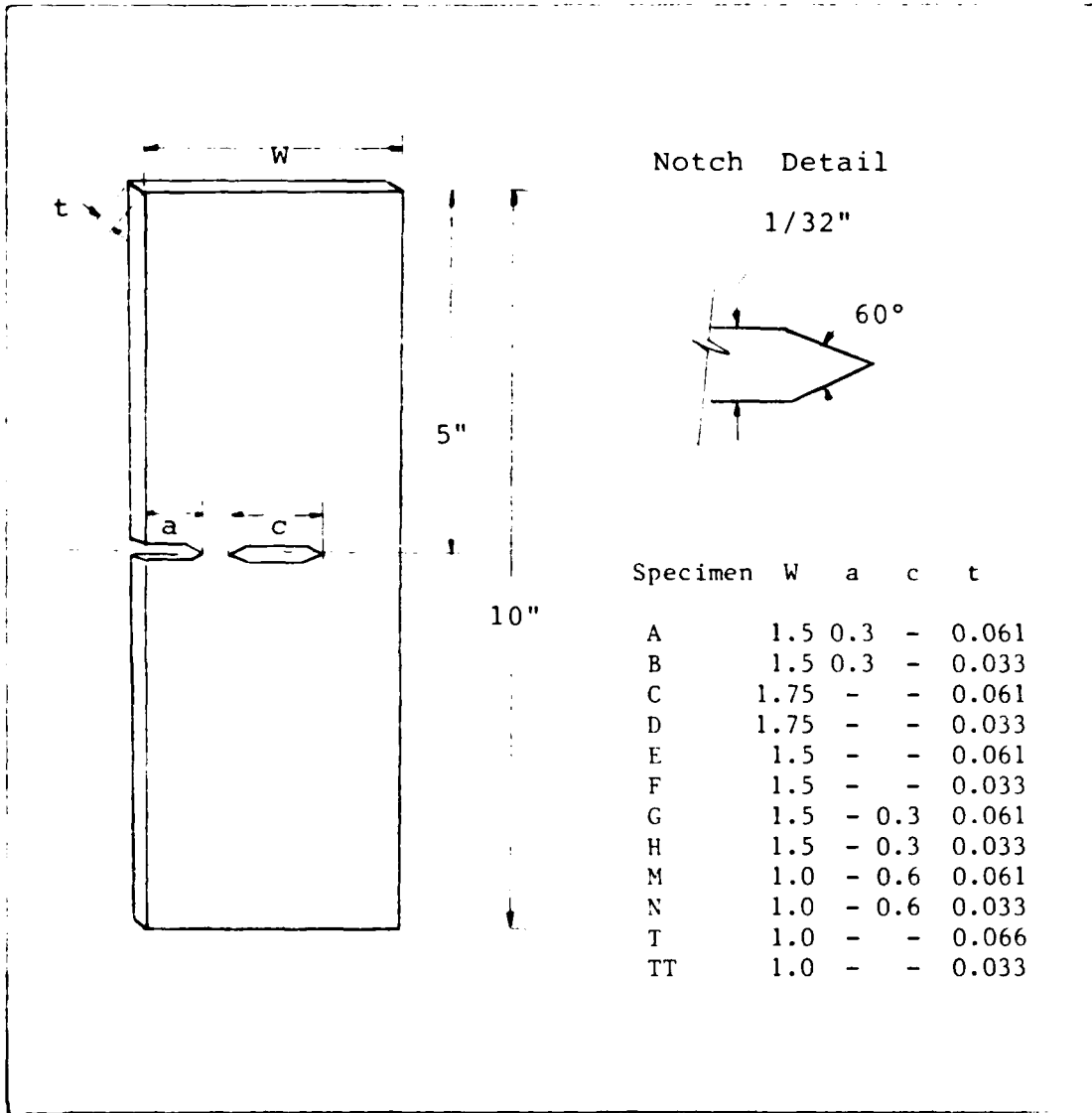


Figure 5. Specimen Design and Labeling Scheme

TABLE I
Experimental Apparatus

Device	MFG	Model	SN	Range	Error
Tensile Machine	Tinius-Olsen				
Tensile Machine	MTS Systems Corp	204.13	187		
Creep Frame	SATEC	C	C-3053-P	12,000	
Load Cell	MTS	661.20A	271	5500 lb	.02%
Load Cell	Interface	1220BF	34279B	25000 lb	1.6%
Extensometer	MTS	632.02B	927	0.1 in	.13%
X-Y Recorder	Hewlett-Packard	7045B	4174	10 U/in	
Hycam	Redlake	41-0004	MP1225	10000 fps	
Locam	Redlake	51-0003	1146	500 fps	
Visicorder	Honeywell	1858	4129		
Strain Gauges	Measurements Group	CEA-13-250UW-350		5 %	.50%
Thermocouples		36 gauge (K-type)		1200° F	4.3%

Fatigue Pre-cracking. The notched specimen were fatigue cracked before being irradiated by the laser so that they would have a sharp crack tip . The specimen were placed in the MTS tensile machine and were cycled in tension at 10 cycles/sec for SEN and 10-30 cycles/sec for CCP specimen. The optimum minimum and maximum loads for each specimen type was found by starting with a low maximum load and slowly

increasing it until a straight fatigue crack 0.01-0.10 inches in length was produced in a reasonable amount of time. Table II is a summary of the optimum loads, number of cycles (N) and fatigue cracked lengths (a).

TABLE II
Fatigue Pre-cracking Details

Specimen Type	Thickness (Code)		Max Load (lb)	Min Load (lb)	N	a (in)
SEN	.061	A	750	70	7500	.03
SEN	.033	B	330	30	10,000	.03
CCP	.061	G	1200	100	14,000	.02
CCP	.033	H	200	20	990,000	.08

Surface Preparation. The specimen were surface buffed to a shiny finish in order to see and photograph the crack better. However, the front surface of a few of the specimen were sanded with 400 grit sandpaper or painted with a high temperature black paint (Duplicolor, High Heat Black DH1602, resistant to temperatures up to 1200°F) in order to produce different rates of energy absorption in the specimen. Since the radiation is in the infrared portion of the electromagnetic spectrum, the deposition of energy on the aluminum is a surface phenomenon (20:1). Therefore, the amount of energy absorbed by the aluminum--hence the heating rate--depends upon the surface treatment of the aluminum.

The shiny samples had an absorptivity of about 1.0 %,

while the sanded samples had an absorptivity about 2.7 % and the painted samples had an absorptivity of about 20 %. A description of the energy coupling calculations is given later.

Instrumentation. Each sample was instrumented with one or two strain gauges (CEA-13-250UW-350) manufactured by Micromasurements Corp. The heated samples had 3 chromel-alumel thermocouples made by spot welding 36 gauge wire to the back surface of the specimen as shown in Figure 6. The number of thermocouples was limited by the available spaces in the visicorder.

High Temperature Tests

Laser Operations. The floor plan of the LH MEL test area is shown in Figure 7. The laser located at LH MEL is a 15 kW CO₂ laser which radiates at an infrared wavelength of 10.6 μ m. The laser power was continuously monitored using the torpedo calorimeter and periodically calibrated using the ballistic calorimeter. Laser spot size at the surface of the test specimen was adjusted by moving the focusing mirror closer to or farther from the specimen. Figure 8 is a photograph of the Plexiglas beam impressions used to verify the spot size. The impressions are made by placing the Plexiglas plate in the target plane and irradiating it for a very short amount of time (about 0.1 second). As can be seen in Figure 8, the beam size remained constant at 12.0 cm² in area from day to day and throughout the test series. In order to control the number of variables, the spot size was

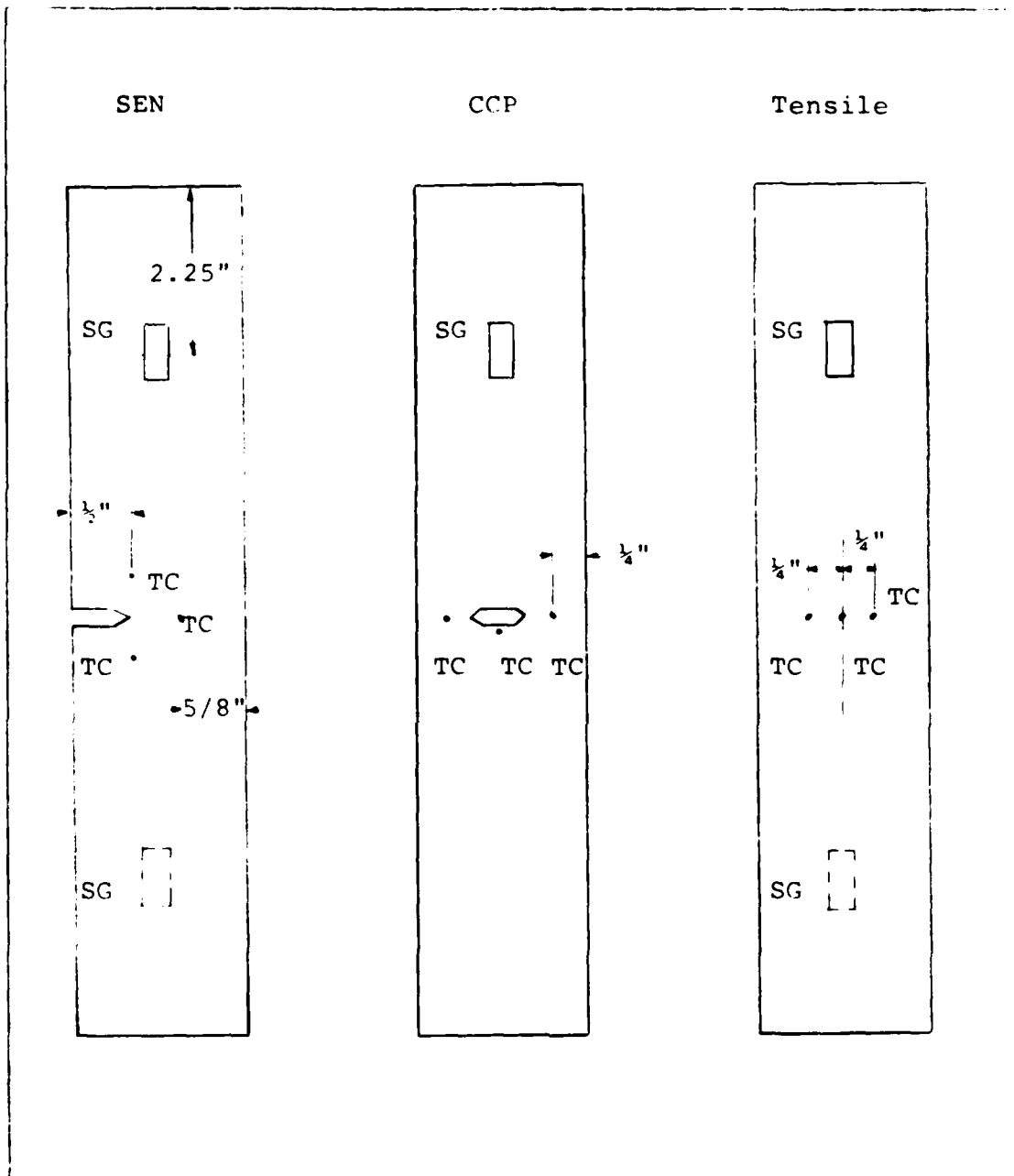


Figure 6. Specimen Instrumentation
 SG - Strain Gauge
 TC - Thermocouple

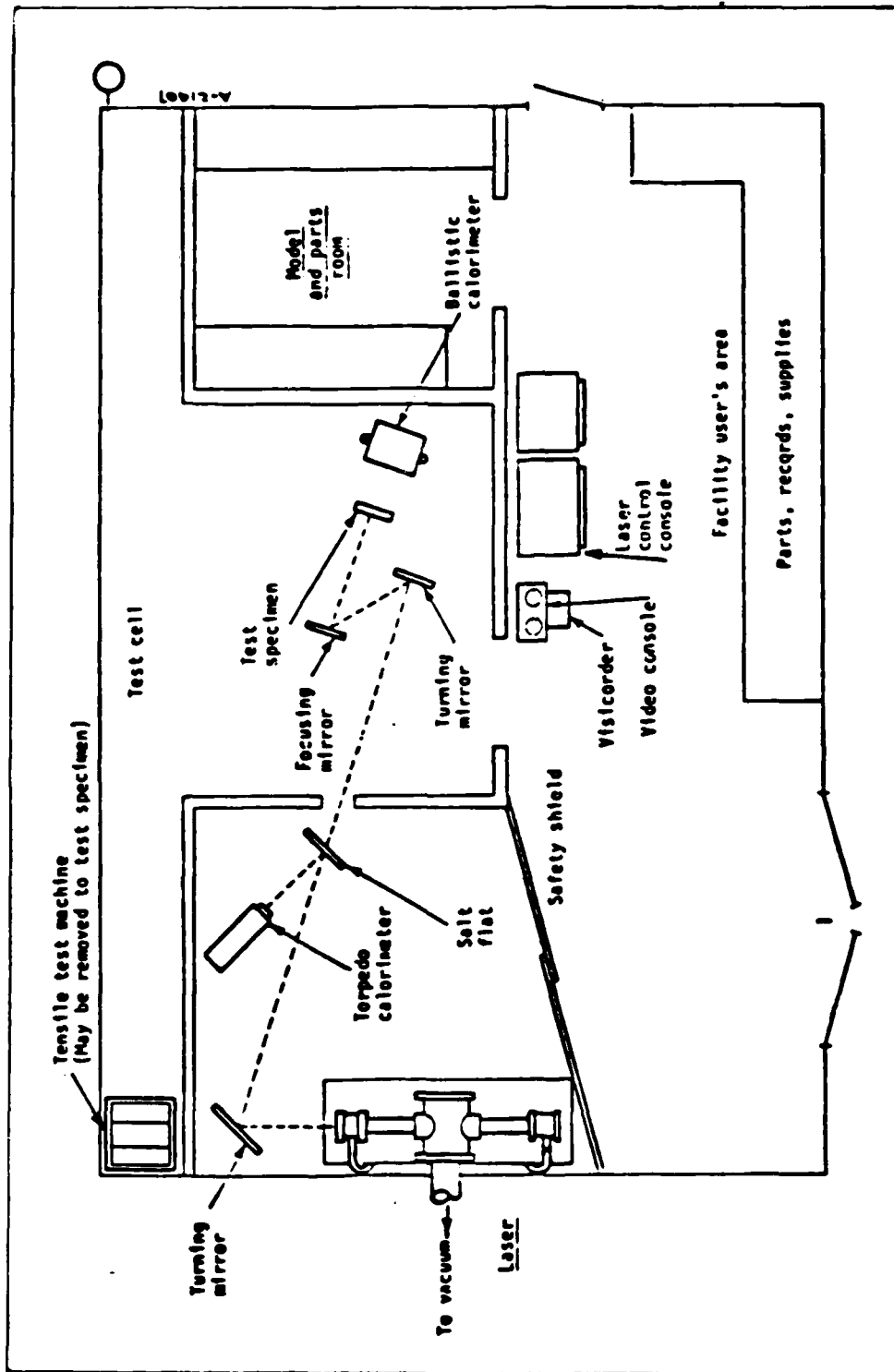


Figure 7. LHMEI Test Cell Lay-out (4)

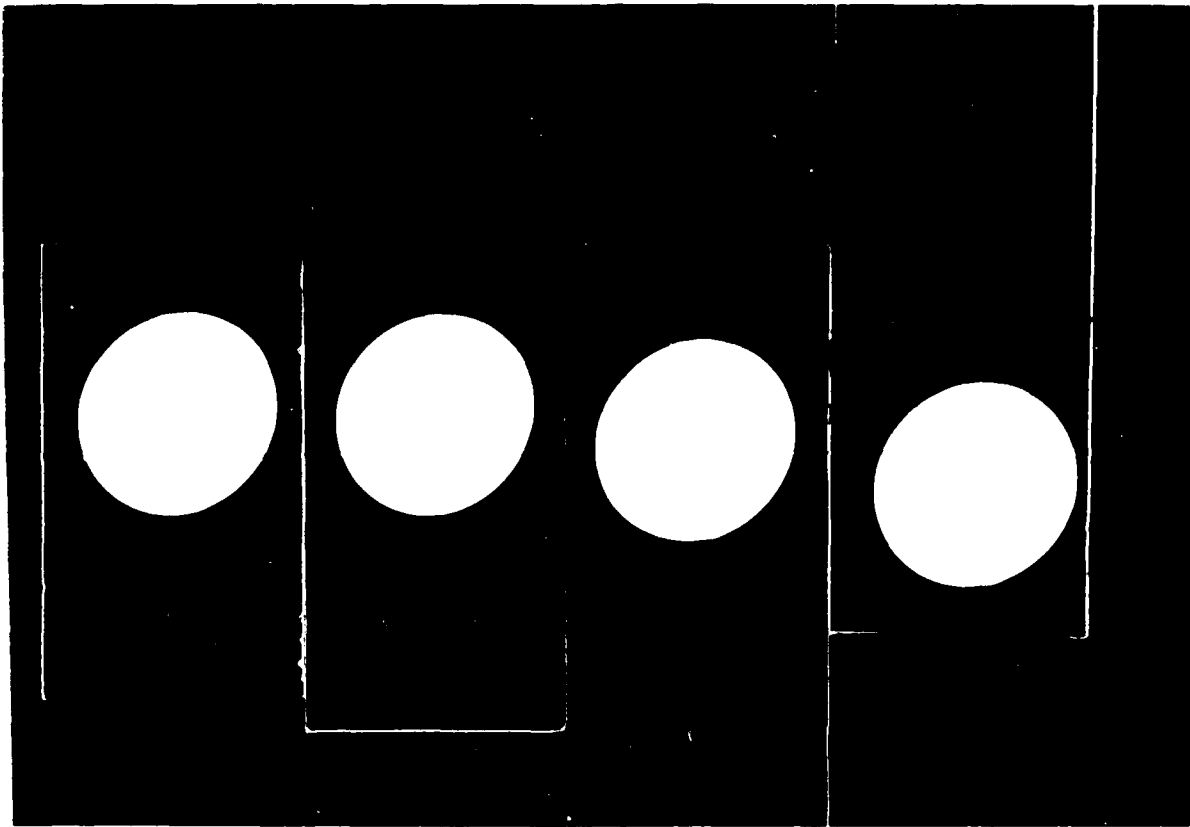


Figure 8. Plexiglas Beam Impressions

chosen such that the entire width of the specimen would be covered by the beam. This was done to keep the temperature along the line of crack propagation as uniform as possible, and to insure that any thermal stresses, caused by rapid thermal expansion in the heated zone, act along the same direction as the applied load.

The incident intensity of the laser energy was varied by increasing or decreasing the laser power. Intensity, I , was determined using the equation

$$I = \frac{P}{A} \quad (13)$$

where

- P = laser power (kW)
- A = laser spot size (12.0 cm²)

The intensity, along with the surface coupling, determined the temperature rise in the metal--recall equation (12), $q = I\alpha$. Three heating rates were considered in this study--low, medium, and high. Table III lists the heating rate ranges for each designation.

TABLE III

Heating Rate Designations

	Typical (°C/sec)	Actual Range (°C/sec)
Low	15	15-40
Medium	150	80-180
High	1500	1000-2500

The LHMEL laser beam is ideal for this type of test because of the flat intensity profile known as a top hat

because the intensity rises sharply at the edge of the beam and remains relatively flat across the interior of the beam. Licata, in his AFIT Thesis (15:47) examined the LHMEEL beam and found that the spatial intensity profile varied only 11-15 percent over the entire spot size. Temporal variations are such that even this small variation in intensity is minimized over time so that the energy absorbed by the plate is virtually uniform.

Temperature Measurements. The back surface temperature was measured on the visicorder which recorded the signals from the chromel-alumel thermocouples. Aluminum has a relatively large thermal diffusivity when compared to other metals. Because of this, the specimen can be assumed to be at a uniform temperature across the thickness. Torvik (21:6) showed that the following equation for the thermal delay time relates the amount of time necessary for the back of the plate to receive information about the temperature effects of the front.

$$t = \frac{x^2}{2k} \quad (14)$$

where

- x = the thickness
- k = the thermal diffusivity

For the plates used in this experiment, $t = 0.0185$ sec for 0.061 in thick plates and $t = 0.0054$ sec for 0.033 in thick plates. This clearly shows that the temperature response on the rear surface due to laser radiation on the front is instantaneous.

For exposure times at least twice the thermal delay time, the relative temperature from front to back surface can be found using the following equation (21:7):

$$T(x,t) - T_0 = \frac{\alpha I t}{\rho C_p l} + \frac{\alpha I t}{k} \frac{(3x^2 - l^2)}{6l^2} \quad (15)$$

where

- T_0 = initial temperature
- x = distance through the plate
- I = incident intensity
- t = laser exposure time
- l = thickness of the plate
- C_p = specific heat
- k = thermal conductivity
- ρ = density

Since the back surface temperature was measured, this equation was used first to solve for α (coupling coefficient) when $x = 0$ (back surface). Solving for α for each of the surface finishes yielded the following results in Table IV. A detailed description of the energy coupling calculations can be found in Appendix A.

TABLE IV

Average Surface Absorptivities
for 6061 T-6 Aluminum at 10.6 μm

α_{sh}	=	.010 (shiny)
α_{sa}	=	.027 (finely sanded)
α_p	=	.20 (painted)

Next, the equation was used for $x = l$ (flux surface) to solve for the temperature rise on the front. The calculations showed that the front surface temperature was at

most 2% higher than the back surface. In other words, the assumption of uniform temperature through the thickness was reasonable.

The temperature profile across the width of the specimen was also assumed to be uniform. In reality though, the middle of the specimen had the highest temperature. This was the temperature that was recorded as the failure temperature. Although the intensity profile of the laser is flat and the beam covered the width of the specimen, such things as heat conduction away from the heated zone and extensometer tabs protruding into the beam caused a reduction in temperature moving out from the center of the beam. The greatest drop off in temperature was seen when testing the SEN specimen with the extensometer tabs. To protect these tabs a notched piece of graphite block was placed in front of the tabs to shield them from the laser radiation while the crack tip was irradiated. In this case, the two thermocouples above and below the crack tip were observed to be about 19% lower in temperature than the center of the sample. The temperature variation along the line where the crack ran was almost certainly much less than this. For example, when the carbon block and extensometer were removed, the maximum temperature variation was less than 8%. The temperature rise in the center of the plate as a function of irradiation time is shown in Figure 9 for each heating rate.

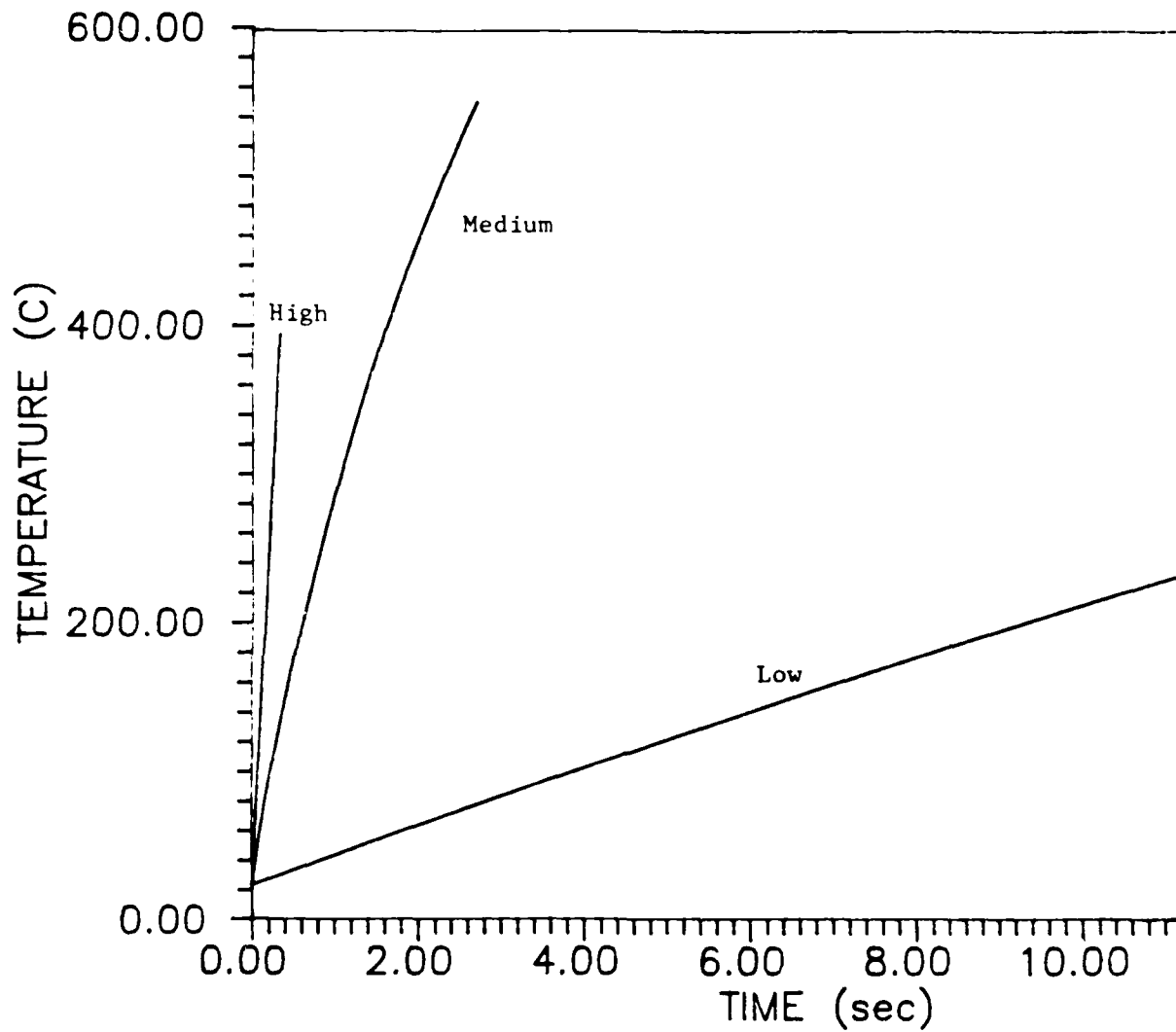


Figure 9. Typical Temperature Versus Time Relation at Center of Plate

Loading. The hydraulic (Tinius-Olsen) tensile machine was initially used to put the samples under load before irradiation. This device proved to be unsuitable because as the material was heated, the displacement due to thermal expansion of the irradiated area caused a rapid decrease in the load. Figure 10 shows a typical decrease in load with time. This figure also shows the decrease of the strength due to temperature rise plotted as a function of time. It can be readily seen that the reduction in load due to thermal expansion was such that the strength, even though decreasing due to a rise in temperature, was always significantly higher than the load. Therefore, there was always a difference between the force available and the force required to drive the crack. Hence, there was no crack growth.

In order to get valid tests, the specimen were tested under the constant load condition using the SAIEC creep frame. A drawing of the creep frame can be seen in Figure 11. The samples were placed in the frame and the dead weight load was applied; and in essence, a rapid heating rate creep test was performed using the laser beam as the heating source. Figure 12 is a photograph of a practice specimen in the loading device after a small amount of crack growth. The extensometer, which was used to measure crack opening displacement, can be seen as well as the flash bulb that was a visual "laser-on" signal which could be seen in the motion picture film.

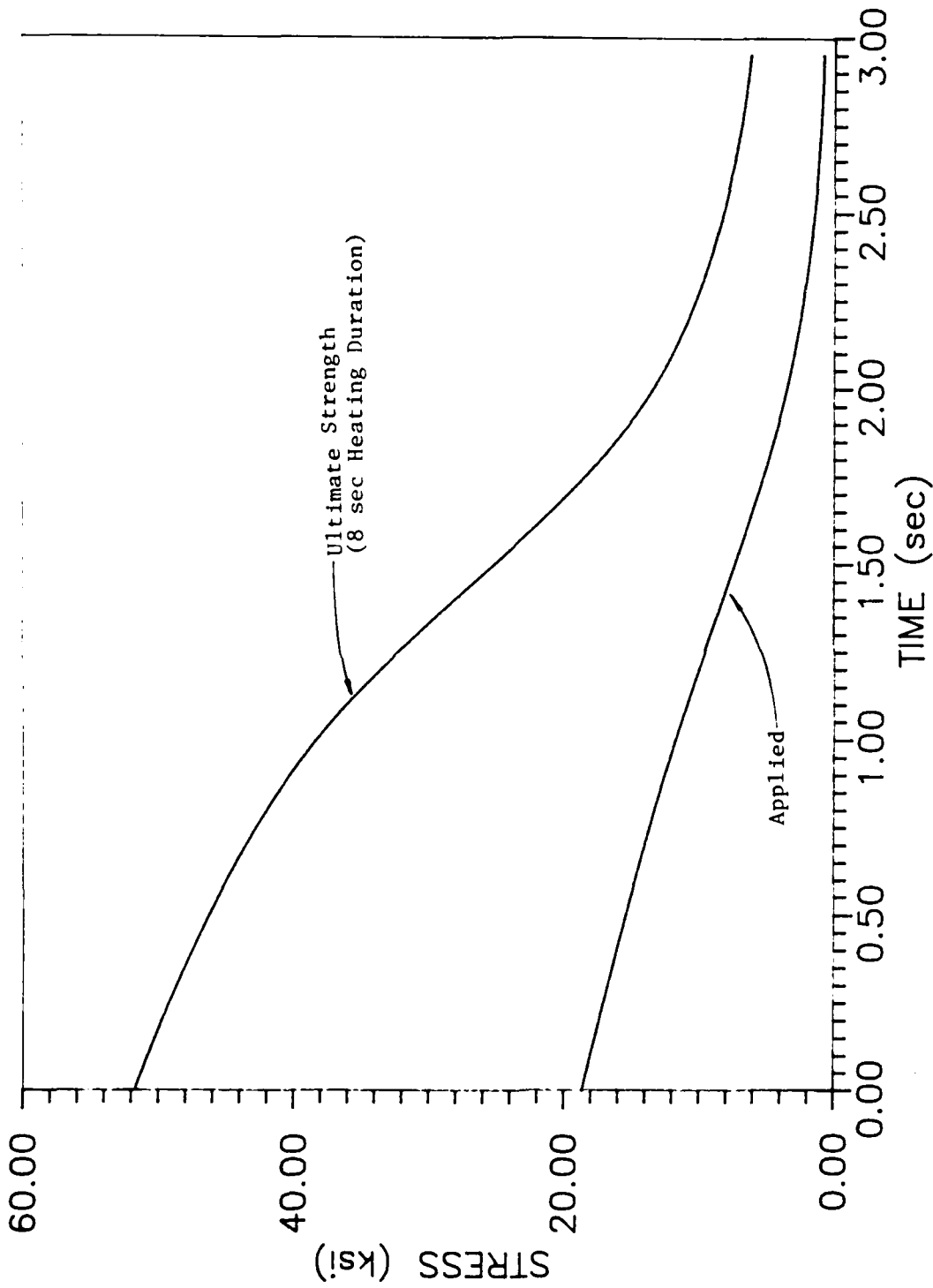


Figure 10. Stress Versus Time Relation During Test with Hydraulic (Tinius-Olsen) Loading Device

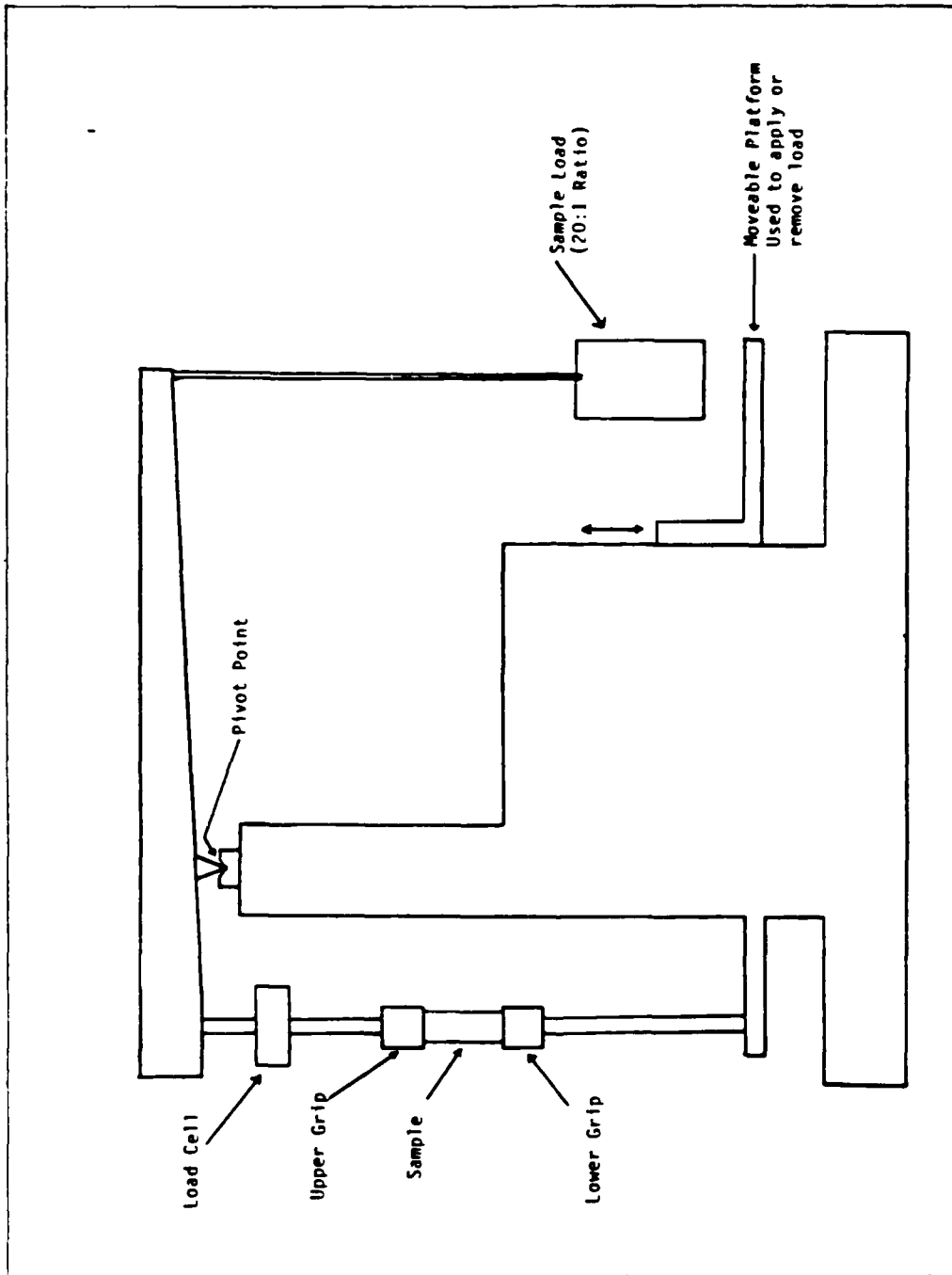


Figure 11. Creep Rupture Tester (SATEC) Drawing (4)

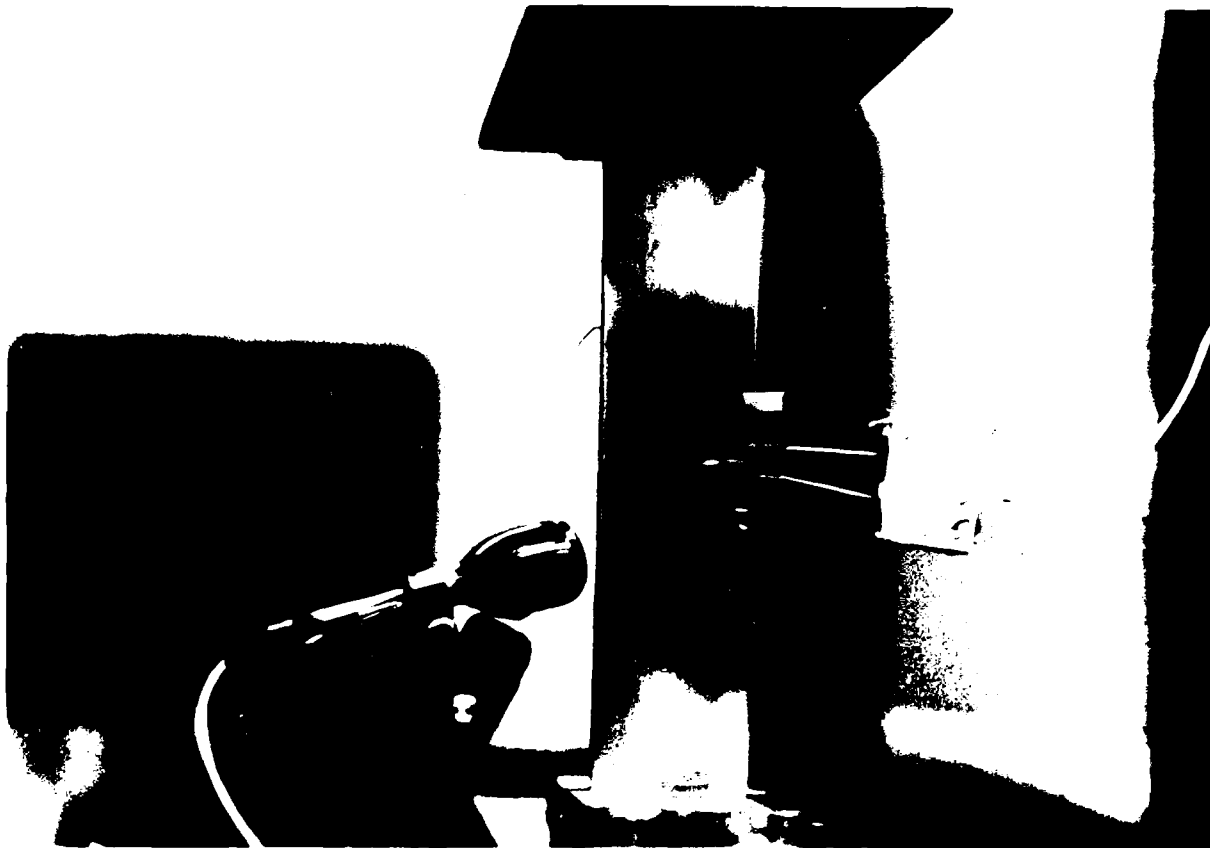


Figure 12. SEN Specimen in Tensile Grips

High Speed (100-500 fps) motion picture of the front and back surface were taken during the test which pinpointed the exact time when the crack began to grow. Figure 13 is a typical load time history for each of the heating rates. For low and medium heating rates, the crack propagation load was virtually constant during the laser irradiation until the crack began to grow. For high heating rates the thermal expansion of the irradiated zone caused an oscillation of the load which was about 15% of the initial load. The oscillation also had a period of between .23-40 sec depending upon the load. For the latter tests, careful review of the film was necessary to determine the onset of crack growth. The failure temperature was considered to be the temperature at the onset of crack growth.

The effective fracture toughness, K_C^* , was calculated based on the initial crack length and the failure load using an expanded version of equation (5) which includes the correction for finite width plates:

$$K_C^* = \frac{L_f}{A} \sqrt{a} \beta \quad (16)$$

where

L_f = the failure load
 A = nominal area of the specimen
 a = crack length

for SEN (7:85)

$$\beta = 1.99 - 0.41\left(\frac{a}{W}\right) + 18.7\left(\frac{a}{W}\right)^2 - 38.48\left(\frac{a}{W}\right)^3 + 53.85\left(\frac{a}{W}\right)^4$$

for CCP (7:85)

$$\beta = \sqrt{\pi} \left(\sec \frac{\pi a}{W} \right)^{\frac{1}{2}}$$

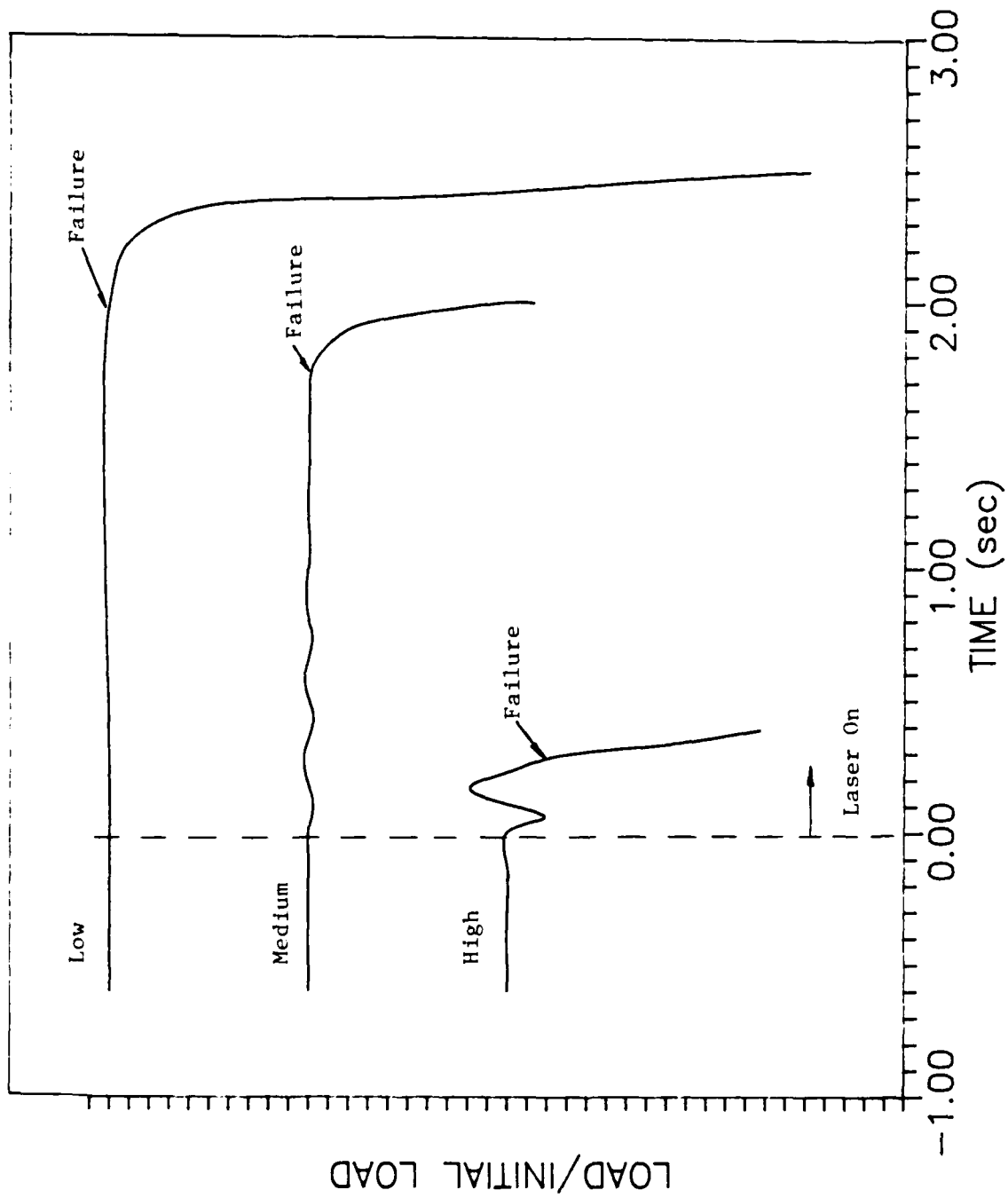


Figure 13. Load Versus Time Histories for Each Heating Rate

Room Temperature Tests

The MIS tensile machine was used for most of the room temperature tests. A few tests were done at LHMEI using the Tinius-Olsen tensile machine. For both the tensile tests and the fracture tests, the Hewlett-Packard X-Y recorder was used to plot load versus displacement. The displacement was measured using the MIS extensometer.

The yield point in the tensile tests was determined by drawing a line parallel to the linear slope of the load-displacement curve beginning at a strain of .002 and intersecting the load-displacement curve as it goes non-linear (2 % offset method). Figure 14 is a typical stress-strain curve. The failure load was considered to be the ultimate load. There was no evidence of large-scale necking which would have resulted in a drop in load before failure. The load was applied manually at a rate designed to fail the specimen in about one second. This corresponded to a strain rate about 10,000 $\mu\epsilon/s$.

Room temperature fracture toughness tests were conducted in the same manner as the tensile tests. However, the point where the load-displacement curve went non-linear was considered to be the critical load for determining the effective fracture toughness. Equation (16) was also used to calculate K_C .

Uncertainty Analysis

Failure Temperature. The uncertainty in the temperature at failure is simply the uncertainty in the temperature

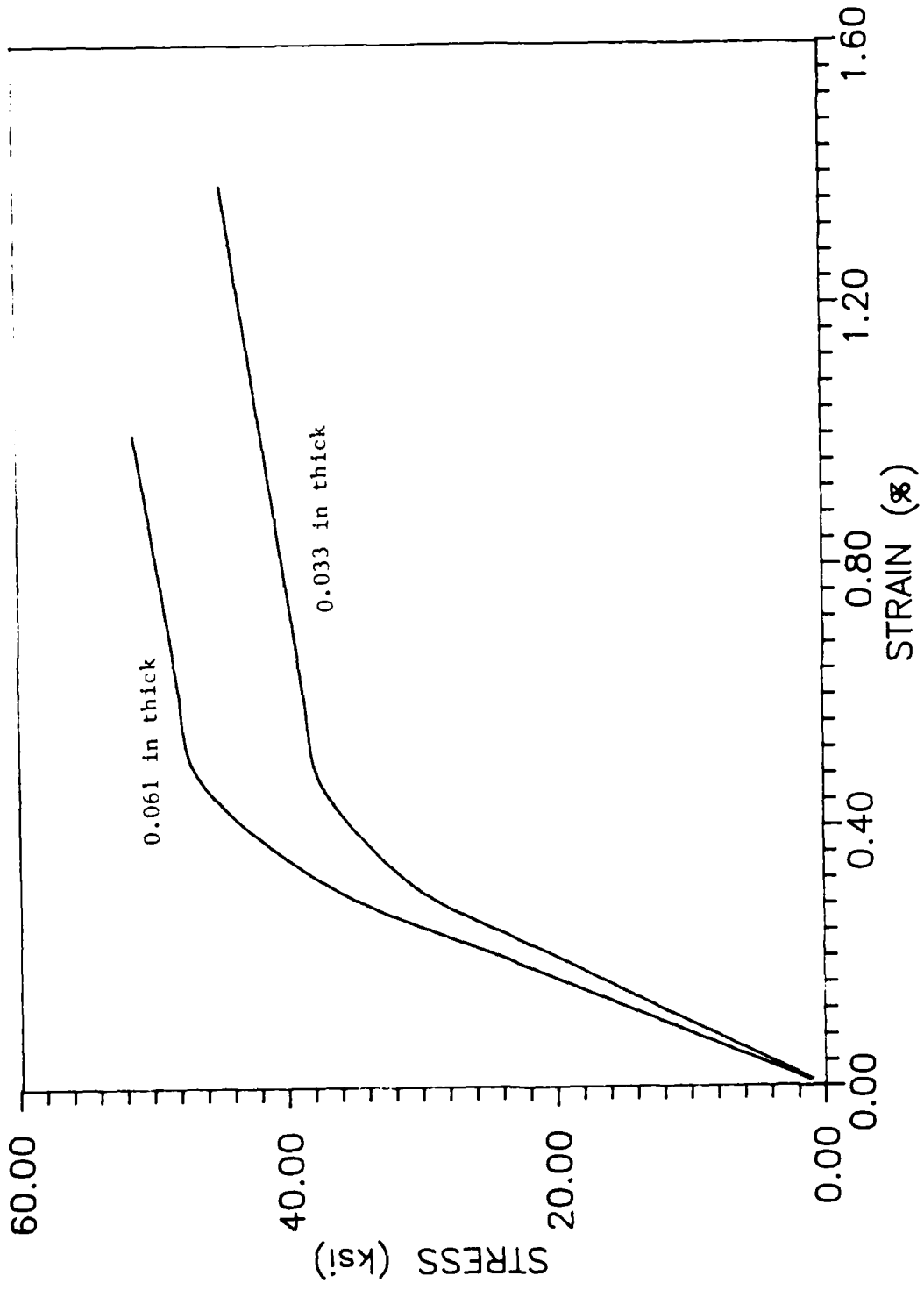


Figure 14. Room Temperature Stress-Strain Curves for 6061 T-6 Aluminum used in Fracture Tests

measurement plus the uncertainty in determining the failure time. The error in the temperature measurement for K-type thermocouples is 4.3% (17:I-25,26). The measurement uncertainty for the failure time is about 0.4% for low and medium heating rates, and 6% for high heating rates. This is based on the motion picture frames necessary to resolve the crack initiation. So, the total uncertainty in temperature measurement goes from 4.7% for heating rates near 15°C/sec to an uncertainty of 10.3% for heating rates around 1500°C/sec.

$\frac{K_C^*}{\sigma_u}$. Using the Kline-McClintock (13:44-46) method to determine the error in the ultimate strength, σ_u , and K_C^* measurements, the errors were calculated to be $\pm 2.4\%$ and $\pm 3.3\%$ respectively.

IV. Results and Discussion

The strength of the aluminum has been shown to be a strong function of temperature and heating rate. Further, strength has an influence on the fracture toughness. Therefore, a number of tensile tests were performed on the aluminum used in the present fracture tests and these results are discussed first. Both room temperature and rapid heating tests were performed. Following the tensile tests, the fracture toughness results are presented along with photographs of the broken specimen and clips from the high speed motion picture film. The data is then analysed according to both linear elastic and ductile fracture mechanics theories.

Tensile Tests

Room Temperature. Tensile specimen of essentially the same configuration (Figure 6) as the fracture specimen--but without the notches--were loaded to failure at a strain rate about 1000 $\mu\text{E/s}$. Eight samples, 0.061 inch thick and seven samples, 0.033 inch thick were tested. The extensometer was used to measure displacement. The 0.2% offset method was used to determine the yield stress. The ultimate stress was assumed to be the failure stress. The linear portion of the stress-strain curve provided Young's Modulus. Table V is a summary of the experimentally determined, average room temperature strength properties of 6061 T-6 aluminum and a

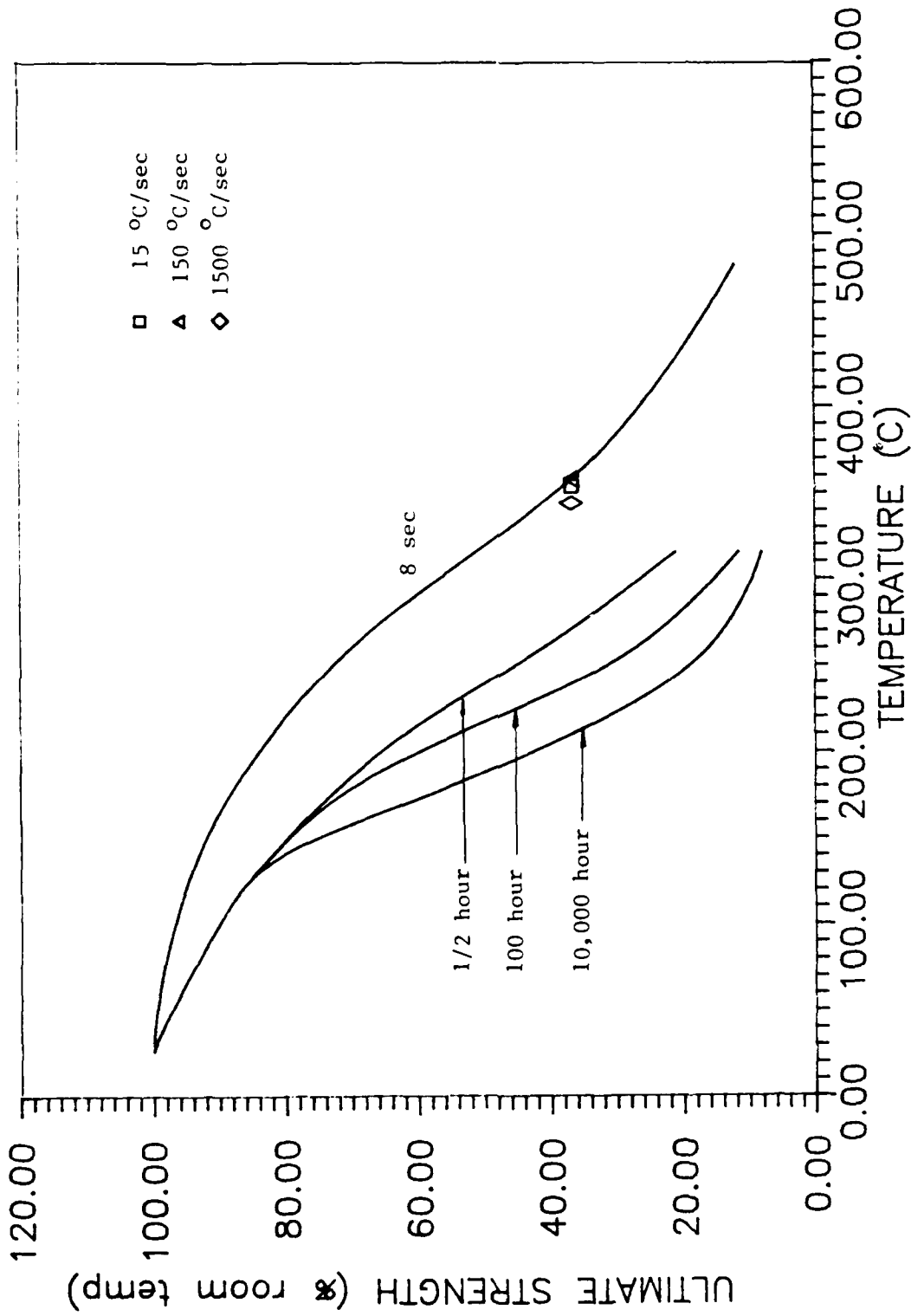
comparison with literature values. For a detailed tabulation of each tensile test, see the data tables in Appendix D.

TABLE U
Strength Properties of 6061 T-6 Aluminum

Thickness (in)	0.033	0.061			
σ_y (ksi)	38.7	48.2	40	38	38
σ_u (ksi)	45.7	51.8	45	41	45
E (10^6 psi)	10.1	11.8	9.9	-	11.1
Source	Present Study	Present Study	(3)	(8)	(10)

The thicker specimen used in the experiments were slightly higher in strength than the handbook values. The thicker samples were 7% higher in yield and 14% higher in ultimate strength than the thin samples.

High Temperature. Three rapid heating tensile tests were conducted using the LHMEI laser. The results of these tests are plotted along with MIL Handbook (8:3-229) and LMSC (10:23) data in Figure 15. All three tests were with 0.061 inch thick specimen. All data in Figure 15 are normalized to the room temperature ultimate strength. The tests were done at the three heating rates used throughout the experiments--low (15°C/sec), medium (150°C/sec), and high (1500°C/sec). It is interesting to note that while the strength seems to be higher as the heating rate gets faster, it appears that the data from this experiment clusters around the 8 second heating rate data.



Effect of Temperature on the Ultimate Strength of 6061 T-6 Aluminum (8:3-229; 10:23)

While it is easy to distinguish between, say, 10,000 hr soak and 8 second soak, there appears to be no distinction between 1/2 second data and 20 second data. Therefore, the ultimate strength for the heating rates considered in these experiments is a function of temperature only; it is not a function of heating rate.

The broken specimen showed evidence of brittle failure at room temperature, and ductile failure for the rapid heating tensile tests. Figures 16 and 17 are photographs of the front views of the specimen and close-up views of the fractured surfaces. The high heating rate test showed considerable necking accompanied with the fracture.

Fracture Tests

Room Temperature. The same experimental procedure used to perform the room temperature tensile tests was used for the room temperature fracture toughness tests. Both single edge notched specimen (SEN) and center cracked panels (CCP) were tested. The average room temperature K_C^* values for the SEN and CCP are shown in Table VI.

TABLE VI

Room Temperature Fracture Toughness for 6061 T-6
(Width = 1.5 in)

Thickness [in]	K_C^* ksi*sq $\sqrt{\text{in}}$	
	SEN	CCP
.033	41.7*	24.7*
.061	46.8*	31.3*

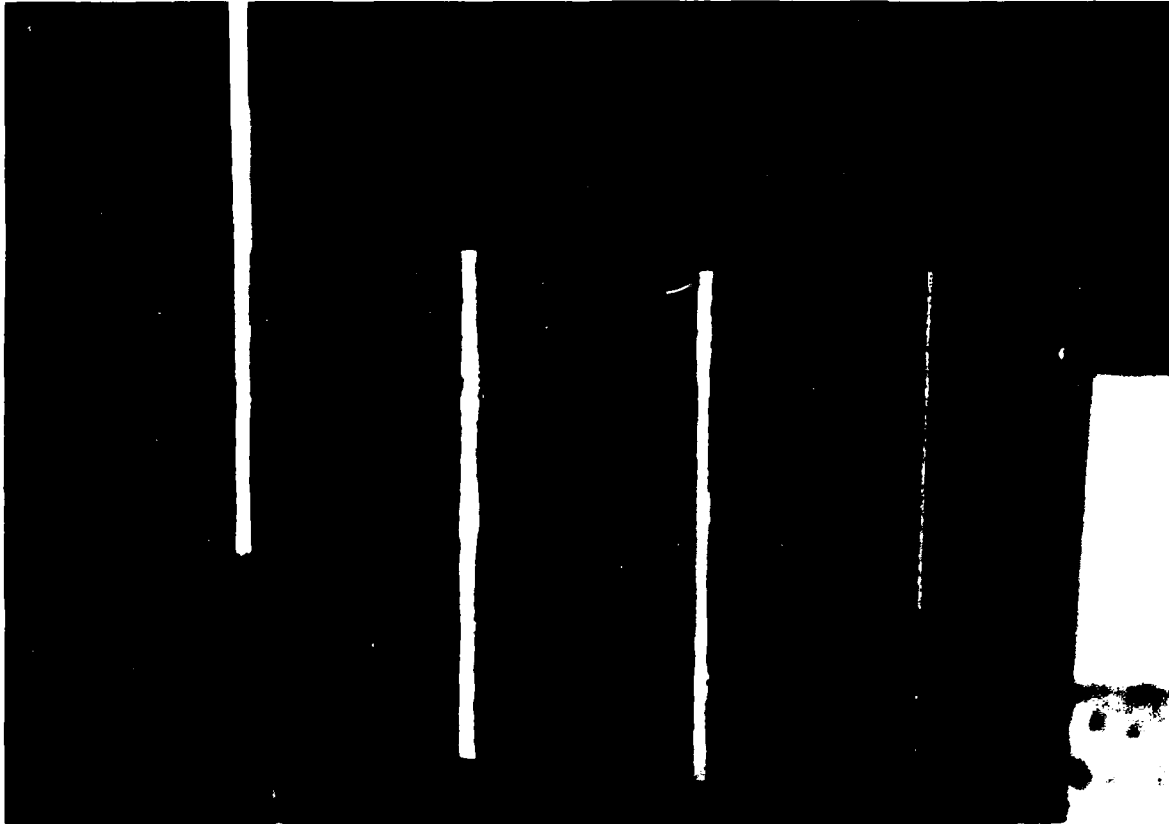
* Failure stress exceeded 80% of yield stress.



(a) (b) (c) (d)

Figure 16. 6061 T-6 Aluminum Tensile Specimen--
After Tensile Test

- (a) Room Temperature
- (b) Low Heating Rate
- (c) Medium Heating Rate
- (d) High Heating Rate



(a) (b) (c) (d)

Figure 17. 6061 T-6 Aluminum Tensile Specimen--
Fracture Surfaces After Tensile Test

- (a) Room Temperature
- (b) Low Heating Rate
- (c) Medium Heating Rate
- (d) High Heating Rate

All specimen failed at stresses greater than 80 % of the yield strength. This fracture behavior is typical of 6061 T-6, and was noted in the Damage Tolerant Design Handbook (1:7.14-3) for tests done on CCP of 4 and 15 inches in width. In fracture tests, when the failure stress is near the yield stress the failure is said to be by "net-section yielding." This type of failure is usually accompanied by a lot of plastic deformation near the fracture. Kanninen (14:129-132,546-550) defined the limit load (P_1) for net-section yielding based upon slip line theory for an elastic-perfectly plastic CCP specimen as

$$P_1 = 2 B b \sigma_y \quad (17)$$

where

- B = thickness
- b = remaining ligament ($W - a$)
- σ_y = yield strength

and for SEN

$$P_1 = 1.072 C B b \sigma_y \quad (18)$$

where

$$C = [1 + (a/b)^2]^{1/2} - a/b$$

Aluminum exhibits strain hardening characteristics at stress levels above the yield point. Therefore, P_1 based upon yield strength in the equations above gives the lower bound of failure load as it assumes an elastic-perfectly plastic material. The upper bound would be a limit load based upon the ultimate strength (P_u). Figure 18 is a plot

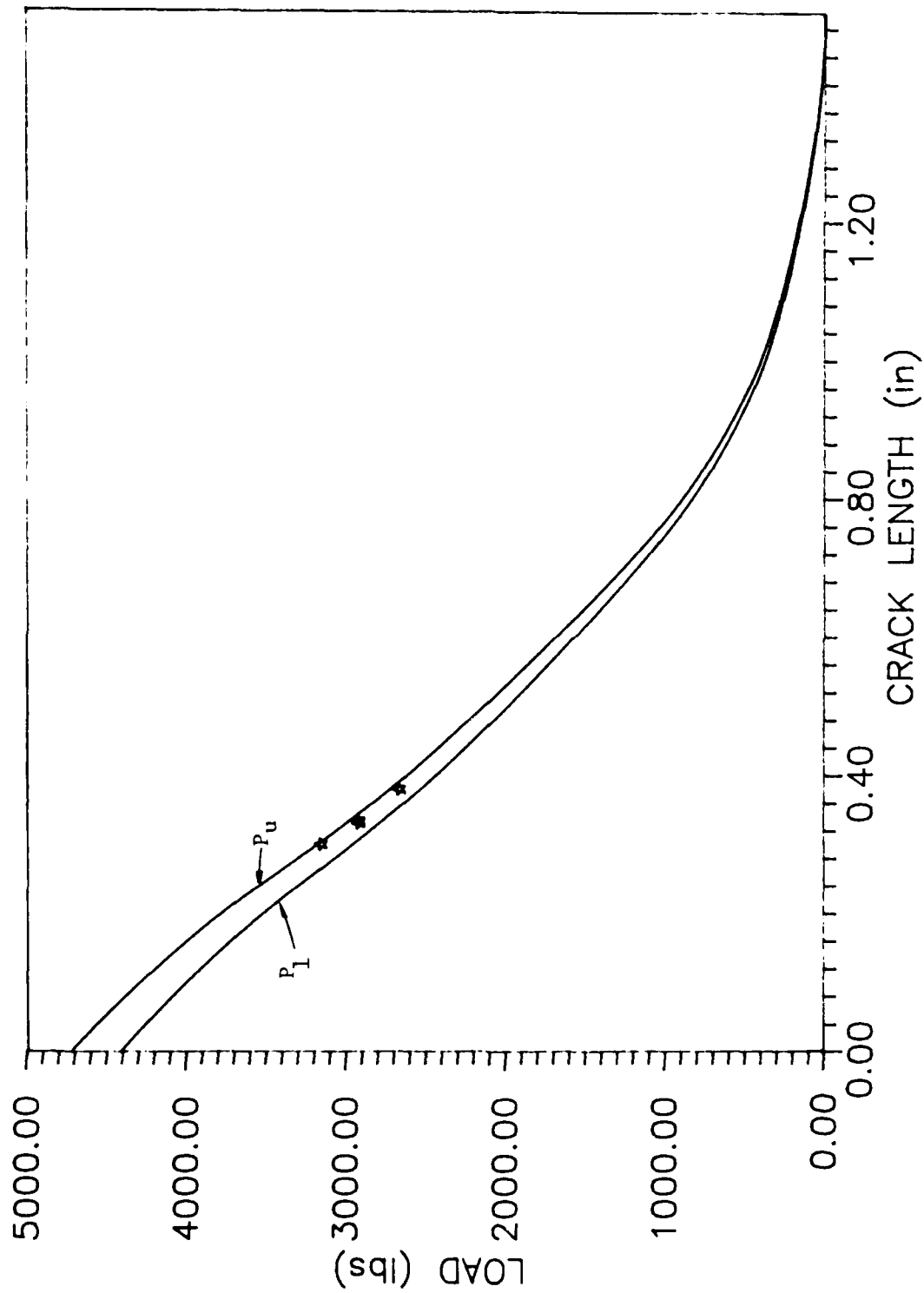


Figure 18. Room Temperature Failure Loads and Net-Section Limit Loads Versus Crack Length for SEN, 0.061 in thick, 1.5 in wide, 6061 T-6 Aluminum

of the measured room temperature failure loads for the 0.061 in thick SEN specimen as a function of crack length. The limit load lines based upon σ_y and σ_u from equations (17) and (18) are also drawn on the plot. It can be clearly seen that the data falls between the two limit lines. This figure is typical of the similar plots for the SEN specimen of 0.033 in thick and also the CCP specimen, which are not shown to avoid duplication. However, calculations for P_1 and P_u for each test, based upon the average room temperature strength properties determined earlier, can be found in Appendix D.

High Temperature. These tests were conducted at LHMEI using the laser and creep frame. Three heating rates and three initial loads--20, 50, and 65 percent of the room temperature yield strength--were employed. For the highest heating rates there was a little oscillation in load during the laser irradiation caused by the rapid thermal expansion of the heated zone; in this case, the load at failure was used in the K_C^* calculations. In the other tests, the initial load and failure loads were the same. The failure instant was verified using the high speed motion pictures. Figures 19, 20, and 21 are a series of frames showing before and after crack propagation.



Figure 19. Crack Propagation Sequence in Specimen A-27
 $t = 15.48$ sec (instant of crack growth)



Figure 20. Crack Propagation Sequence in Specimen A-27
 $t = 15.65$ sec



Figure 21. Crack Propagation Sequence in Specimen A-27
 $t = 15.78$ sec

Figure 22 is a plot of K versus temperature relation for the 0.033 inch thick specimen. Figure 23 is a plot of K versus temperature relation for the 0.061 inch thick specimen. All data from each heating rate and specimen were fitted with a regression analysis to give an average K as a function of temperature. This is represented by the solid line in these figures. The results show no distinction between medium and low heating rates for either thickness.

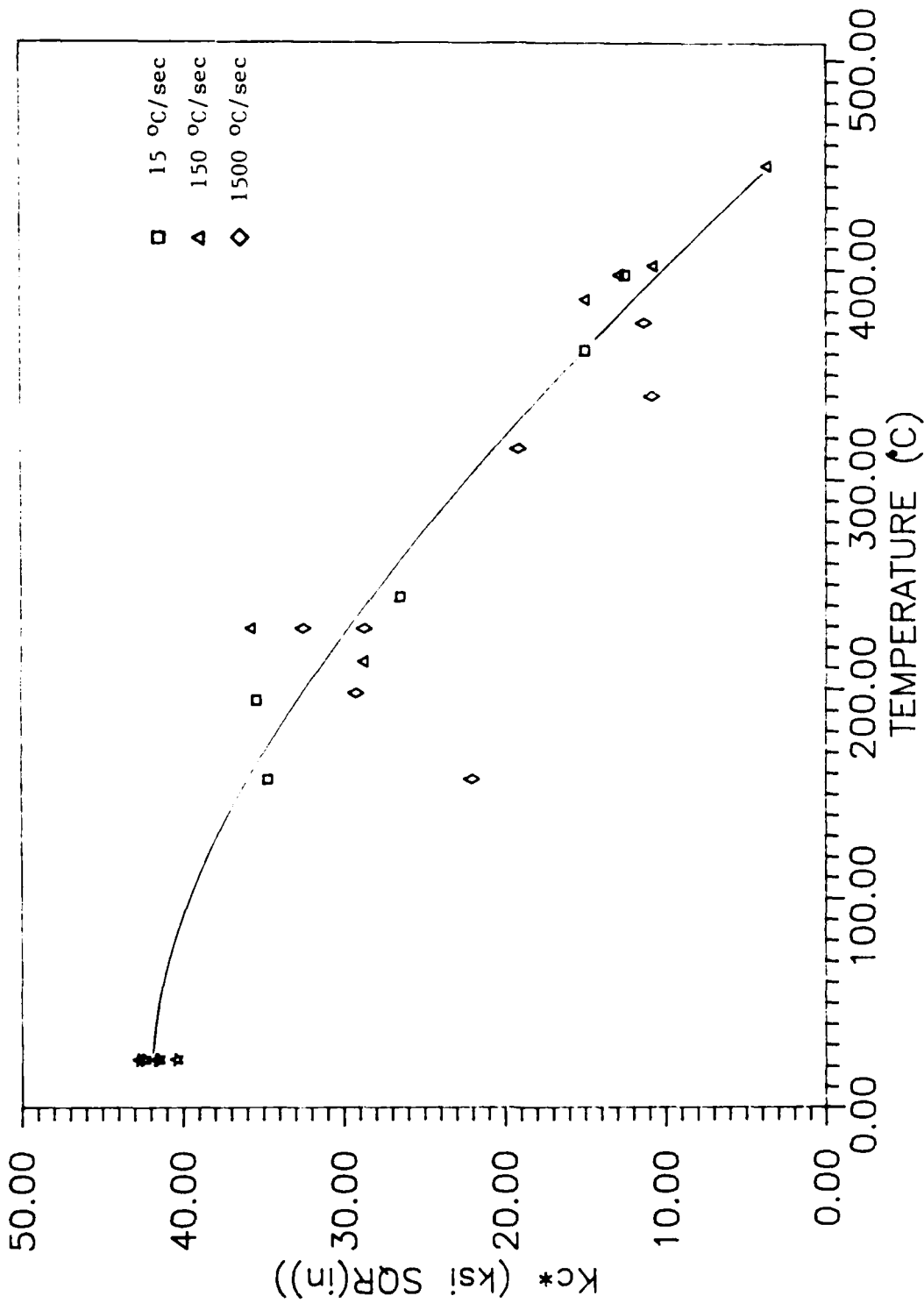


Figure 22. Kc* Versus Temperature Relation for 6061 T-6 Aluminum (0.033 in thick)

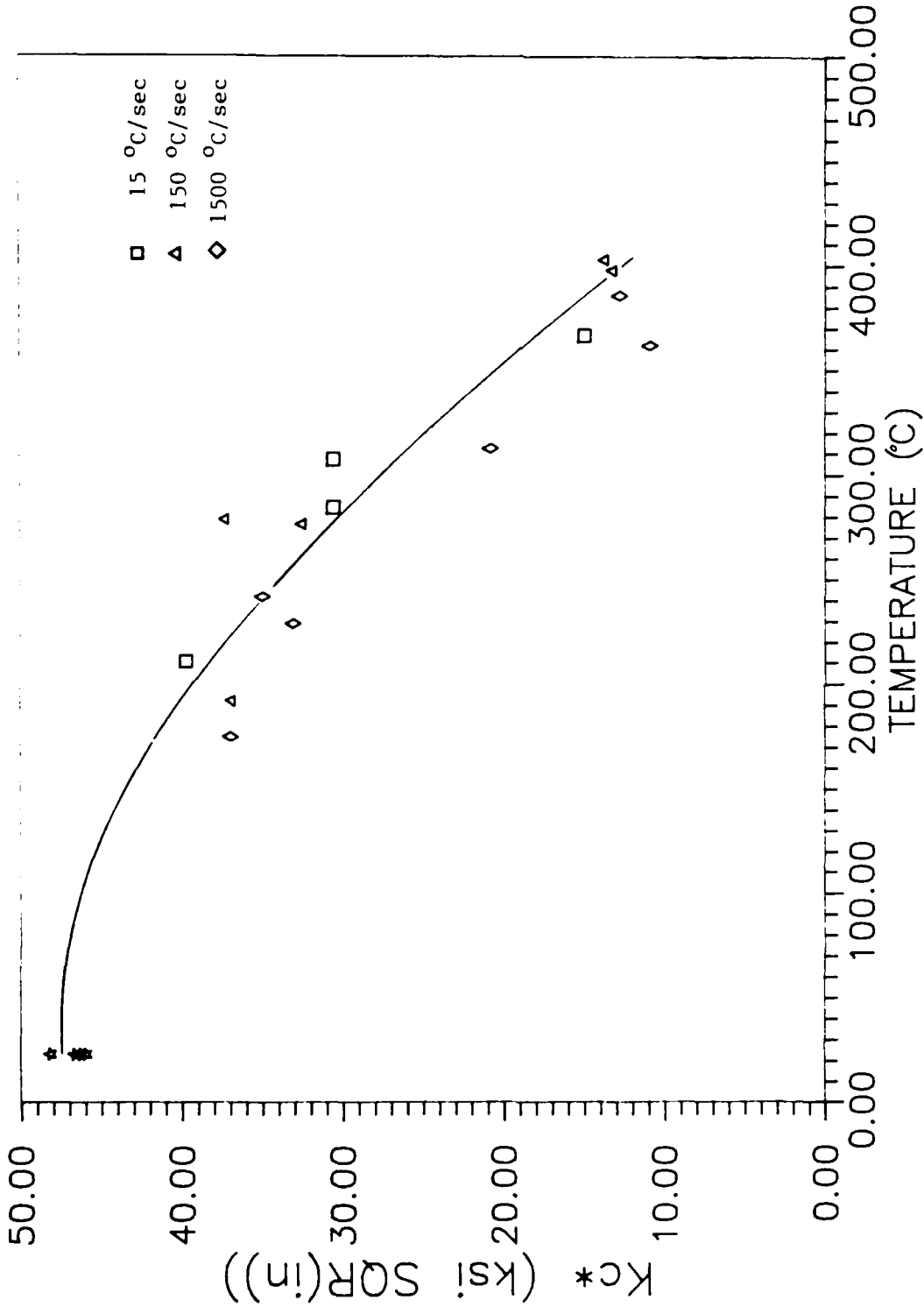


Figure 23. Kc* Versus Temperature Relation for 6061 T-6 Aluminum (0.061 in thick)

The high heating rate tests show K_C^* values slightly below the average. This is more evident in the data from the 0.061 inch thick SEN specimen.

As mentioned previously, the room temperature strength and fracture toughness of the thicker specimen was higher than the thinner specimen. To account for this variation, all K_C^* data from both thickness were normalized with their respective room temperature K_C^* , as shown in Figure 24. The normalization shows no thickness effect between 0.033 and 0.061 inch plates.

A close look at the specimen after failure revealed a significant amount of yielding near the crack surfaces. Figures 25 and 26 are photographs of the SEN specimen after testing. The three specimen shown were all tested at the same load, but at various heating rates. The faster the heating rate the more necking near the crack. Figures 27 and 28 are photographs of SEN and CCP tested at the same heating rates, but at different loads. The load did influence the appearance of the fracture face. The specimen which failed under a high initial load showed less plastic deformation than those that failed under a low load. This observation is not surprising because of the lower temperature at failure for highly stressed plates.

The limit loads for net-section yielding, based upon strength properties which vary with heating rate, showed results similar to those reported for the room temperature tests. Figure 29 shows a typical limit load versus

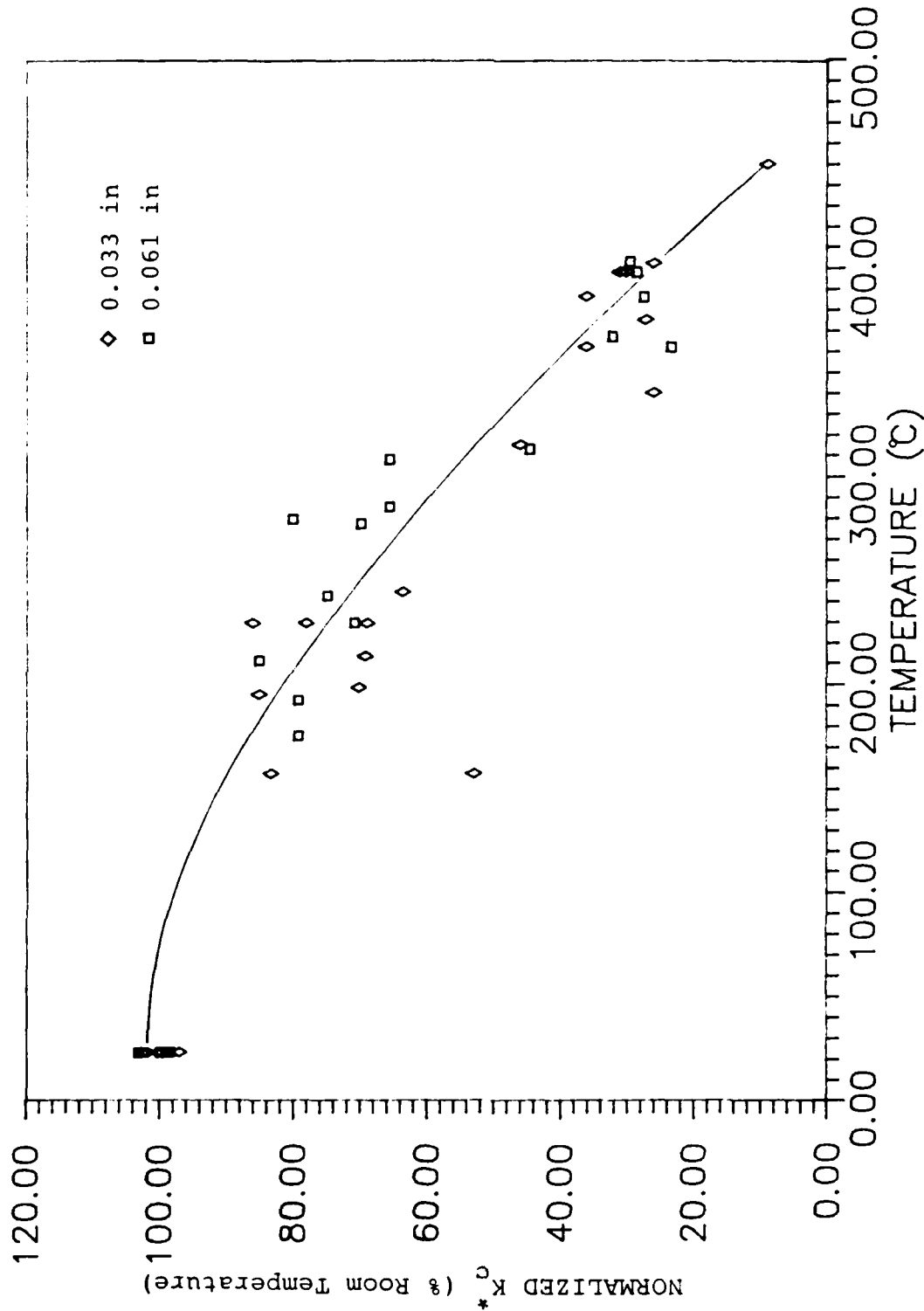


Figure 24. Normalized Kc* Versus Temperature Relation for 6061 T-6 Aluminum



(a)

(b)

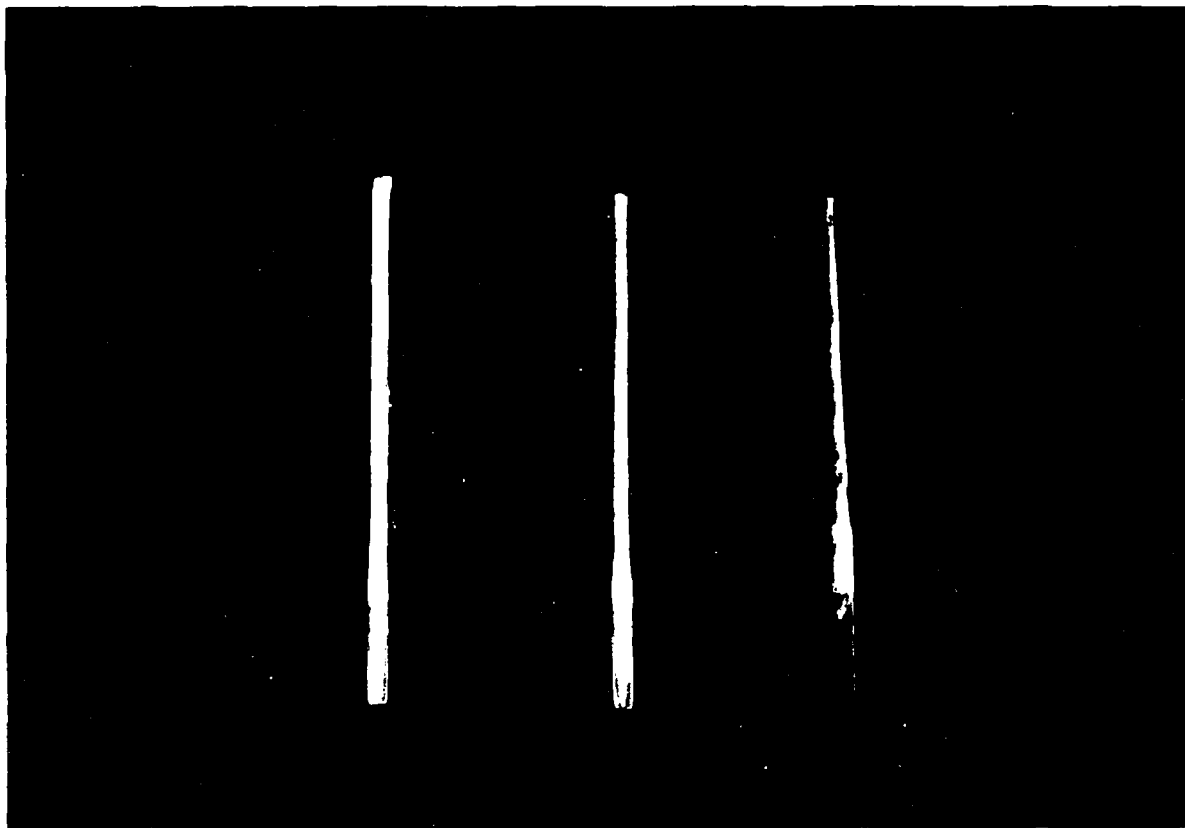
(c)

Figure 25. SEN--After Fracture Test

(a) Low Heating Rate

(b) Medium Heating Rate

(c) High Heating Rate



(a)

(b)

(c)

Figure 26. SEN Fracture Surfaces--After Fracture Test

(a) Low Heating Rate

(b) Medium Heating Rate

(c) High Heating Rate



(a)

(b)

(c)

(d)

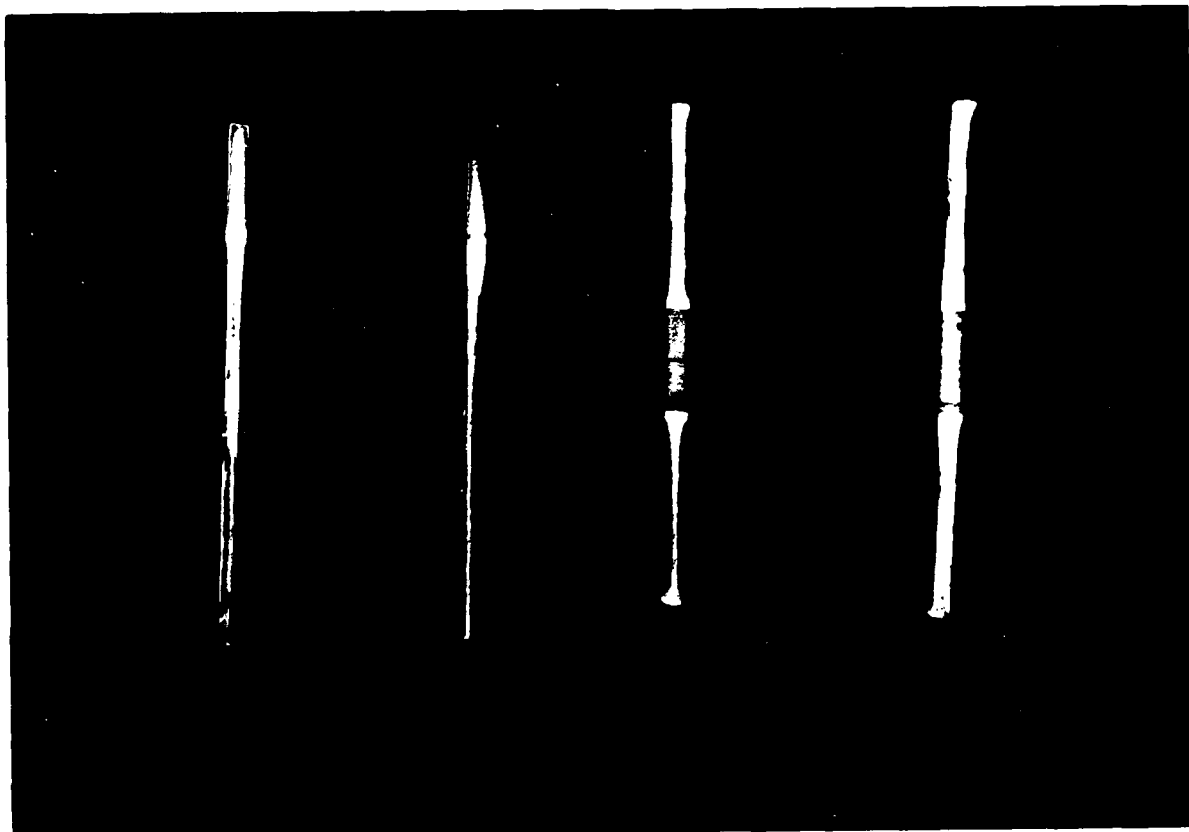
Figure 27. SEN and CCP--After Fracture Tests with Medium Heating Rate

(a) SEN (24.7 ksi)

(b) SEN (8.7 ksi)

(c) CCP (24.7 ksi)

(d) CCP (9.8 ksi)



(a)

(b)

(c)

(d)

Figure 28. SEN and CCP Fracture Surfaces
After Fracture Tests

(a) SEN (24.7 ksi)

(b) SEN (8.7 ksi)

(c) CCP (24.7 ksi)

(d) CCP (9.8 ksi)

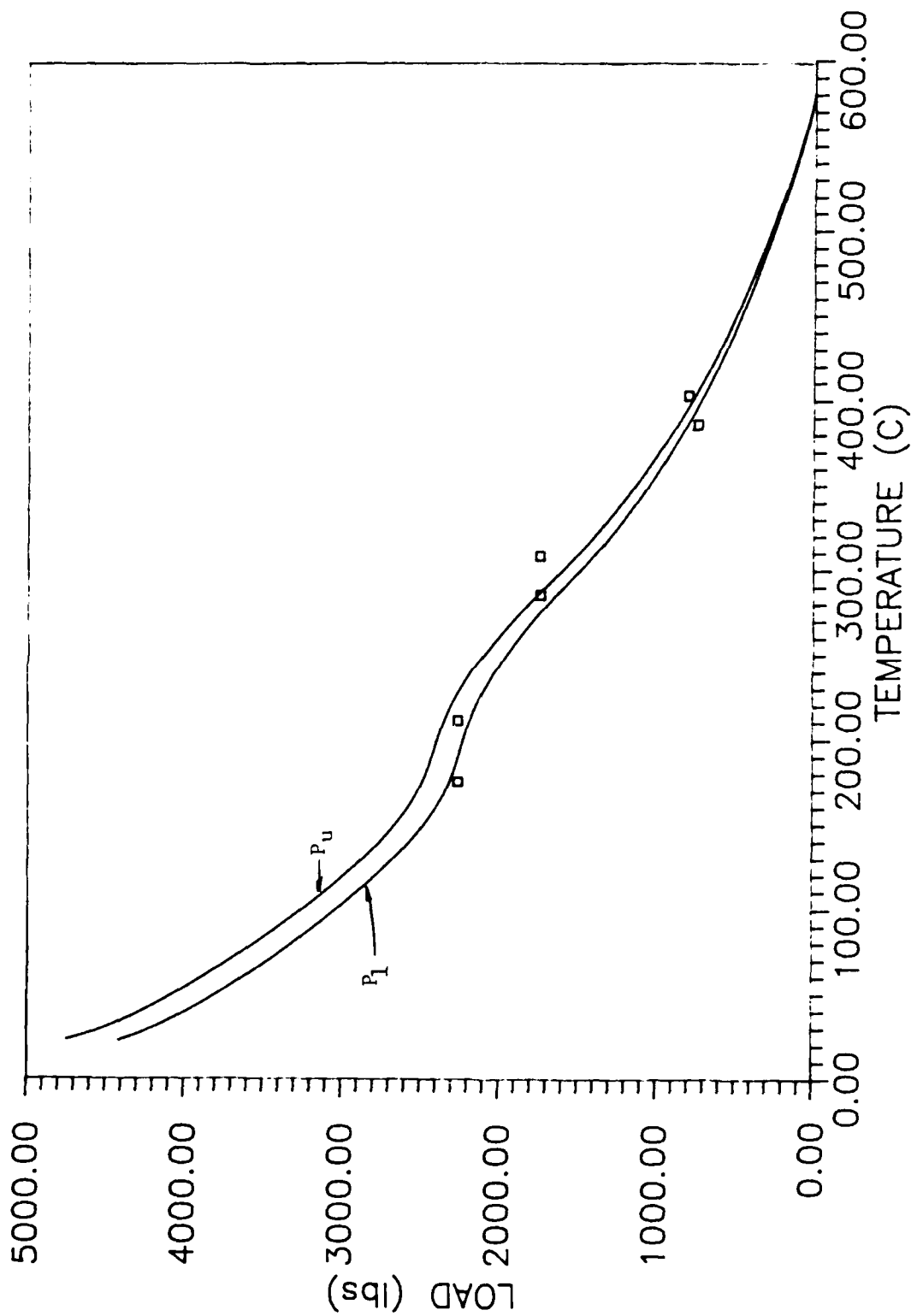


Figure 29. Limit Load Versus Temperature Relations along with Measured Failure Loads for SEN, 0.061 in thick, 1.5 in wide, 6061 T-6 Aluminum, and Average Crack Length = 0.367 in.

temperature relation for SEN, 0.061 inch thick, with an average crack length of 0.367 inches (here, data from specimen with crack lengths between 0.363 and 0.370 only are plotted). As was seen in the room temperature tests, the failure load, in general, falls between the two limit loads. The data from the other specimen configurations yielded essentially the same results and can be seen, for individual tests, in Appendix D.

The evidence of plasticity brings up a question about the validity of employing the effective fracture toughness, K_C^* , a parameter based on a simple extension of linear elastic fracture mechanics. This needs to be investigated further for cases where plasticity is limited. It may require a fracture study with very thick plates or wider plates which would, however, cause thermal stresses along with mechanical stresses due to uneven heating during high heating rate experiments. In other words, there is an obvious need to employ elastic-plastic fracture mechanics. This was shown here, as a first step, with net-section yielding based upon slip line theory. However, a more sophisticated analysis with J-integral, crack opening displacement (COD), or some other fracture parameter might be a more appropriate method for future studies involving elasto-plastic fracture at rapid heating rates. In this direction, a ductile fracture model has been developed by Faramand and Bozich (9). The results of the present study were compared with this model which is discussed next.

Ductile Fracture Analysis

Farahmand and Bozich (9) took the ductile fracture model discussed earlier that was developed by Bockrath and Glassco (5) and modified it for use at high temperatures. Figure 30 is a family of rapid heating stress-strain curves for 6061 T-6 aluminum (10:23). The stress and strain properties from the curves are fed into equation (11) to define the critical crack length as a function of stress. This method is cumbersome to use because it requires iterative solutions to many of the parameters in equation (11). This requires that the solutions be obtained by computer. The methodology used to derive the relationships in equation (11) is covered in Appendix B, and the calculations for critical crack length as a function of stress are located in Appendix C. Figures 31 and 32 are plots of the modified Bockrath-Glassco model using the rapid heating mechanical properties for 6061 T-6 (18). Critical crack length versus failure stress from the present study are also plotted. The data plotted are from specimen which failed in a narrow temperature band above and below the temperature from which the stress-strain properties are known. The plate widths used in the SEN tests are equivalent to a 3 inch wide CCP. The theoretical lines for 3 and 10 inch wide plates as well as for an infinitely wide plate are plotted on the graphs. The results from the present study agree very well with the theoretical calculations from the model. While this approach does not produce a single

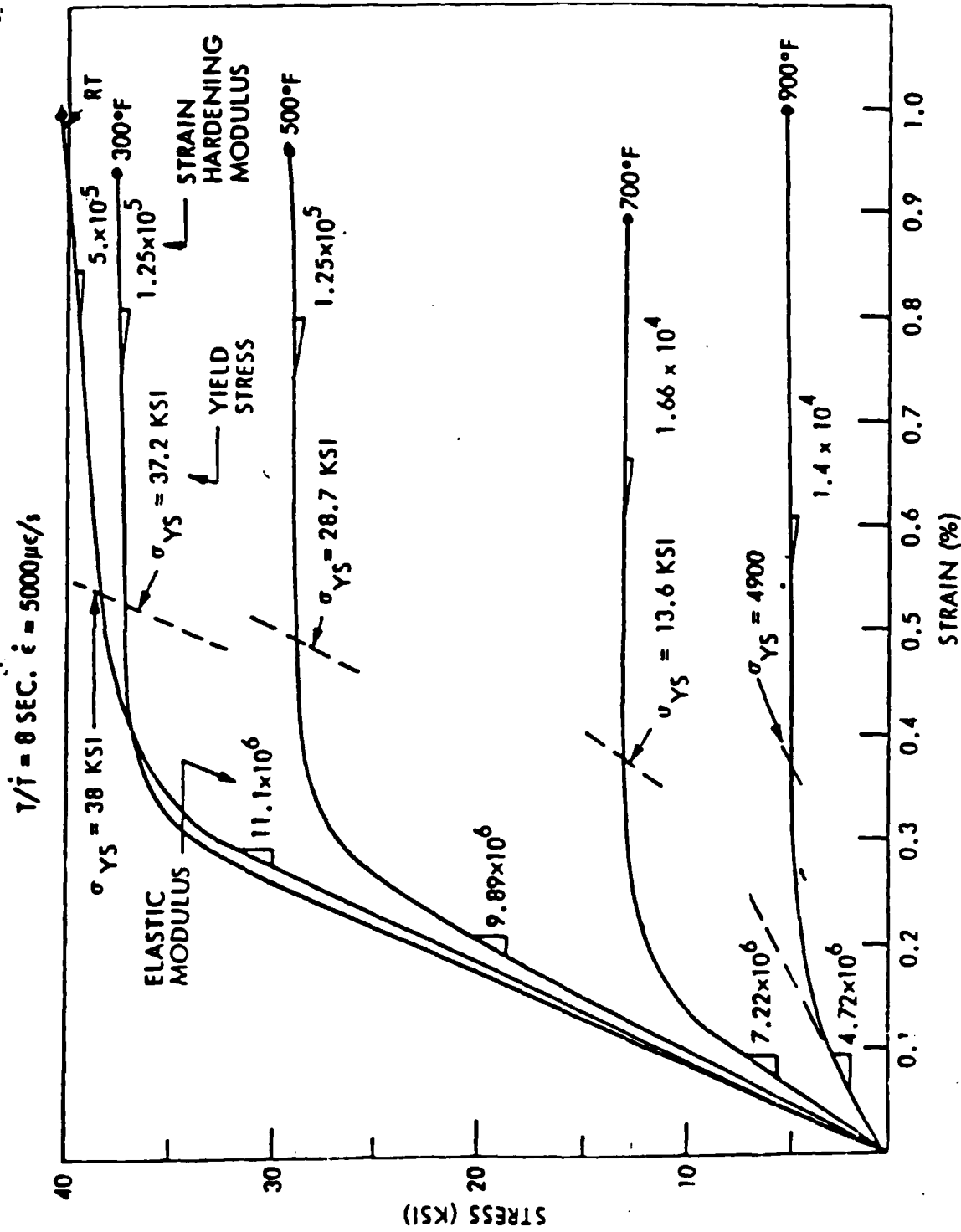


Figure 30. Stress-Strain Curves for 6061 T-6 Aluminum Under Rapid Heating (10)

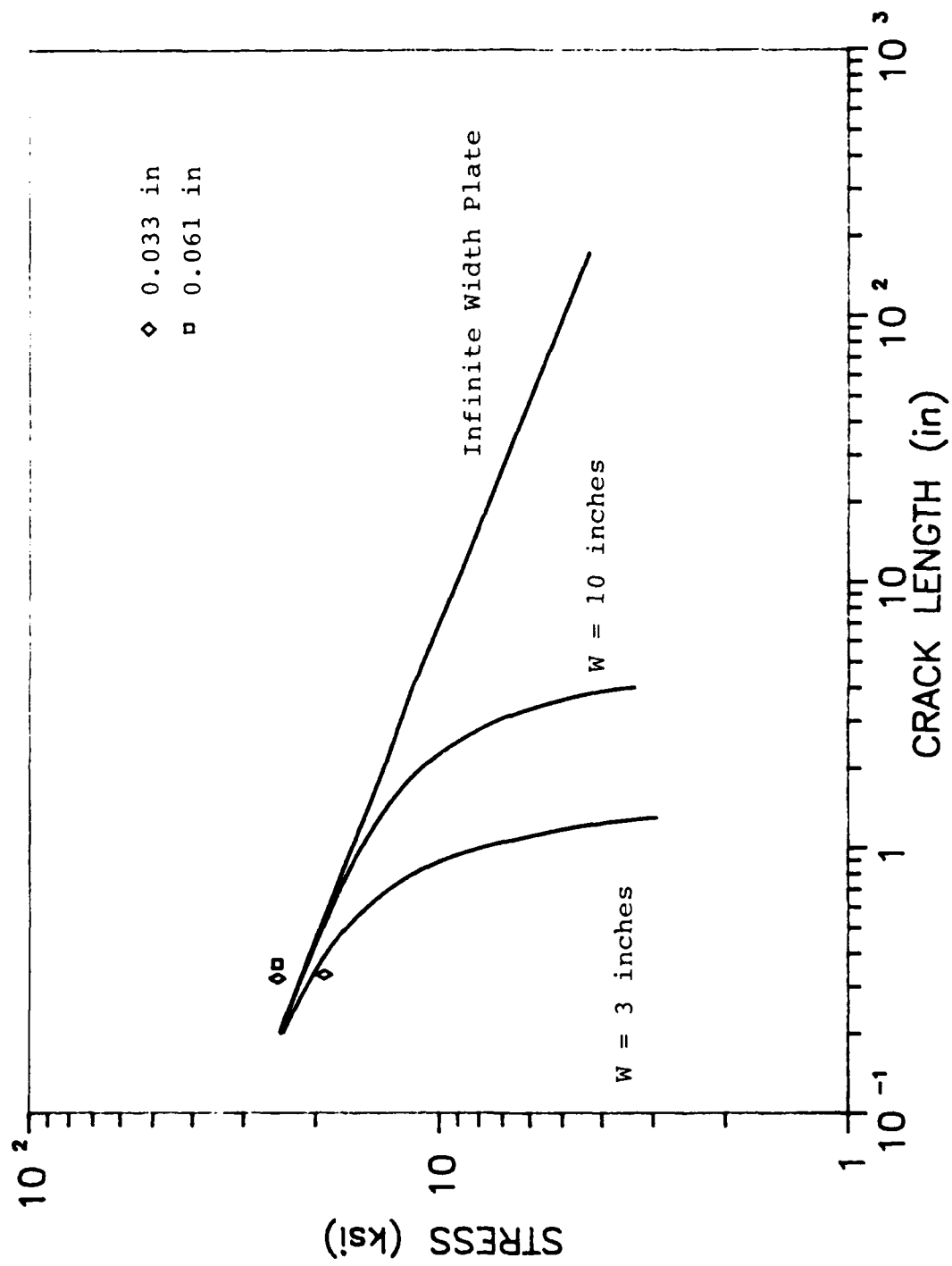


Figure 31. Comparison of Measured Fracture Strength of 6061 T-6 Aluminum with Ductile Fracture Model at 150°C

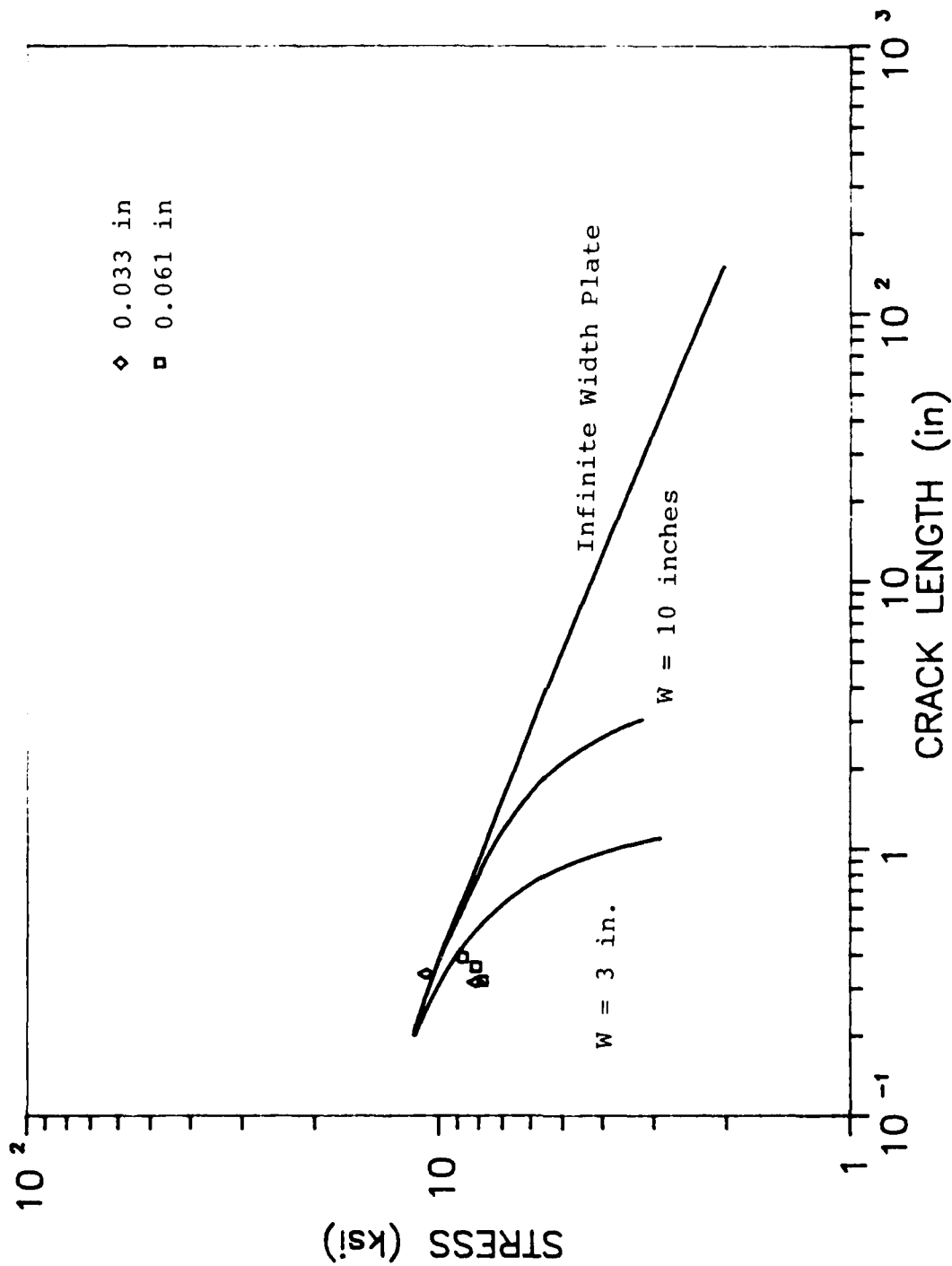


Figure 32. Comparison of Measured Fracture Strength of 6061 T-6 Aluminum with Ductile Fracture Model at 370°C

parameter, like K_C^* , it does provide a relationship between critical crack size and stress for each temperature that rapid heating stress-strain properties are known.

V. CONCLUSIONS

The main objective of this study was to determine the fracture toughness of aluminum as a function of temperature and heating rate. A number of conclusions can be drawn from the experimental results and analysis of this work.

It came as no surprise to find out that the failure was a strong function of the material strength. The strength, in turn, was found to be a strong function of temperature, but rather surprisingly, not a strong function of heating rate. The strength of aluminum has been well established, long before this thesis, to be a function of temperature soak time where creep is involved. These soak times are 1/2 hour or longer. However, in this experiment, for rapid heating tensile tests, where heating rates ranged from 15-1500°C/sec and times to failure were 0.5-20 sec, all of the specimen failed at about the same temperature for the same load.

The effective fracture toughness (K_C^*) was determined by the failure load and the initial crack length. The K_C^* was found to decrease as temperature increased. Like the strength, K_C^* was not a function of heating rate. Even at room temperature, 5061 I-6 aluminum fracture specimen failed primarily by net-section yielding. This means that the K_C^* results may not be used directly to predict failure in wider specimen. Using net-section limit loads based on the ultimate and yield strengths as a function of temperature, effective upper and lower limits of the failure stress could be determined. In retrospect, a more brittle aluminum would

have been a better material to study if rapid heating rate properties were known. Although, even with a brittle aluminum, the results at high temperatures are likely to be strongly influenced by plasticity near the crack tip.

A good model for predicting critical crack length as a function of stress at elevated temperatures was the modified Bockrath-Glassco ductile fracture mechanics approach. This model, while cumbersome to use because of the rapid heating rate stress-strain properties needed, showed good agreement with the experimental results of this thesis.

As for applying this work to the failure of pressurized cylinders, a couple of statements can be made. If either the flaw size or the internal pressure is known, an estimate for the critical value of the other quantity can be made using the modified Bockrath-Glassco method. In this study, every effort was made to simplify the stresses in the material. The temperature was kept uniform across the width of the specimen so that there would not be thermal stresses or bulging and a uniaxial tension load was the only applied stress. A more complete investigation would begin by testing with biaxial stress and with spot sizes which do not cover the width of the plate so that the effects of thermal expansion could be identified. Another factor that was not investigated at all in this thesis was subcritical crack growth. In order to fully understand the laser-pressurized shell problem a more complete understanding of how the crack initiates and grows to critical length in the midst of rapidly changing temperatures is important.

APPENDIX A: Thermal Coupling and Through-Thickness Temperature Calculations

This section outlines the calculations performed which determined the coupling of laser energy into the aluminum specimen, and the variation in temperature through the thickness of the specimen. In all of the calculations the thickness used is 0.061 inches--the thickest specimen. So, the calculations are for the worst case in terms of error. The calculations are based upon a one-dimensional heat conduction equation from Torvik (21:7):

$$T(x,t) - T_o = \frac{\alpha I t}{\rho C_p l} + \frac{\alpha I t}{k} \frac{(3x^2 - l^2)}{6l^2} \quad (15)$$

where

- T_o = initial temperature
- x = distance through thickness of plate
- I = incident laser intensity
- t = laser exposure time
- l = plate thickness
- C_p = specific heat
- k = thermal conductivity
- α = coupling coefficient
- ρ = density

Coupling Coefficient

The back surface temperature was measured. So, to find the coupling coefficient, equation (15) can be simplified by setting $x = 0$ (assumes an insulated back surface).

$$T(0,t) - T_o = \frac{\alpha I t}{\rho C_p l} - \frac{\alpha I t}{6k} \quad (19)$$

where

- $T = 23 \text{ }^\circ\text{C}$
- $l = 0.061 \text{ in}$
- $C_p = 0.96 \text{ J/g}^\circ\text{C} \quad (22)$

$$k = 1.67 \text{ W/cm } ^\circ\text{C} \quad (22)$$

$$= 2.70 \text{ g/cm}^2 \quad (22)$$

Sample Calculations using Equation (19).

1. Sample A31 (shiny surface, low heating rate)

$$T(0, 10.4) = 211^\circ\text{C}$$

$$I = 400 \text{ W/cm}^2$$

$$(211-23) = 26310\alpha - 2.44\alpha$$

$$\alpha = 0.00715$$

2. Sample A22 (shiny surface, medium heating rate)

$$T(0, 1.87) = 192^\circ\text{C}$$

$$I = 1000 \text{ W/cm}^2$$

$$(192-23) = 11827\alpha - 6.09\alpha$$

$$\alpha = 0.0143$$

3. Sample A26 (finely sanded surface, medium heating rate)

$$T(0, 1.71) = 279^\circ\text{C}$$

$$I = 1000 \text{ W/cm}^2$$

$$(279-23) = 10815\alpha - 6.09\alpha$$

$$\alpha = 0.0237$$

4. Sample A30 (painted surface, high heating rate)

$$T(0, 0.15) = 229^\circ\text{C}$$

$$I = 1000 \text{ W/cm}^2$$

$$(229-23) = 948.7\alpha - 6.09\alpha$$

$$\alpha = 0.219$$

Through-Thickness Temperature Variation

With the coupling coefficient solved, set $x = 1$ (flux surface) in equation (15):

$$T(1,t) - T_o = \frac{\alpha I t}{\rho C_p l} + \frac{\alpha I t}{3k} \quad (20)$$

Sample Calculations using Equation (20).

1. Low Heating Rate (Sample A31)

$$\alpha = 0.00715$$

$$T(1,10.4) = 188.1 + 0.017 + 23 = 211.1^\circ\text{C}$$

$$T(0,10.4) = 211.0^\circ\text{C}$$

$$T(\text{back})/T(\text{front}) = 0.9994$$

2. Medium Heating Rate (Sample A22)

$$\alpha = 0.0143$$

$$T(1,1.87) = 169.13 + 0.174 + 23 = 192.3^\circ\text{C}$$

$$T(0,1.87) = 192.0^\circ\text{C}$$

$$T(\text{back})/T(\text{front}) = 0.9984$$

3. High Heating Rate (Sample A30)

$$\alpha = 0.219$$

$$T(1,0.15) = 207.76 + 2.66 + 23 = 233.4^\circ\text{C}$$

$$T(0,0.15) = 229^\circ\text{C}$$

$$T(\text{back})/T(\text{front}) = 0.9811$$

APPENDIX B: Calculation Procedure for Computing the Critical Crack Length using Ductile Fracture Mechanics

Faramand and Bozich (9) modified the ductile fracture mechanics method developed by Bockrath and Glassco (5) for use in predicting the critical crack size in metals at elevated temperatures. In this section, the steps needed to calculate the theoretical crack length as a function of stress and plate geometry are provided. Equation (1), which was introduced earlier, states the basic theory developed by Griffith (5:10) and expands it to include the energy consumed in plastic straining at the crack tip, U_p . The failure criterion becomes

$$\frac{\partial}{\partial a} (U_e - U_s - U_p) = 0 \quad (6)$$

From LEFM, the elastic energy release rate is

$$\frac{\partial}{\partial a} U_e = \frac{\pi \sigma_u^2 a}{E} \quad (2)$$

where σ_u and E are taken from the stress-strain curve. Also from LEFM, the energy required to create new crack surfaces is

$$\frac{\partial}{\partial a} U_s = 2T \quad (7)$$

where

$$T = 5.634 E^{-10} \text{ (for aluminum)}$$

Finally, the plastic strain energy rate is defined as

$$\frac{\partial}{\partial a} U_p = w_f h + w_u h \quad (8)$$

where

- w_f = the plastic strain energy absorption rate above the ultimate stress at the crack tip.
- w_u = the plastic strain energy absorption rate below the ultimate stress in the region surrounding the crack tip.
- h = height of strained region at crack tip.

Equation (6) can now be rewritten after substituting equations (2) (7) and (8) as follows:

$$a = \frac{E}{\pi \sigma^2} [2I + w_f h_f + w_u h_u] \quad (21)$$

The w_f is determined based on the amount of energy absorbed by the slip band at the crack tip. While w_u is the unrecoverable energy under the uniaxial stress-strain curve from σ to σ_u . These two quantities can be determined from the material stress-strain curve. Figure 33 shows the relationship between w_f and w_u for different types of stress-strain curves. The high temperature analysis of 6061 aluminum simplified because the stress-strain curve is similar to (b) in Figure 33. The ultimate and failure stresses and strains are the same. Therefore

$$w_f = 0 \quad (22)$$

From equation (9) the above relations indicates that

$$\epsilon_{pn} = 0.$$

The bulk of the computations are needed to calculate the unrecoverable strain energy under the stress-strain curve from the applied stress to the ultimate stress ($w_u h_u$).

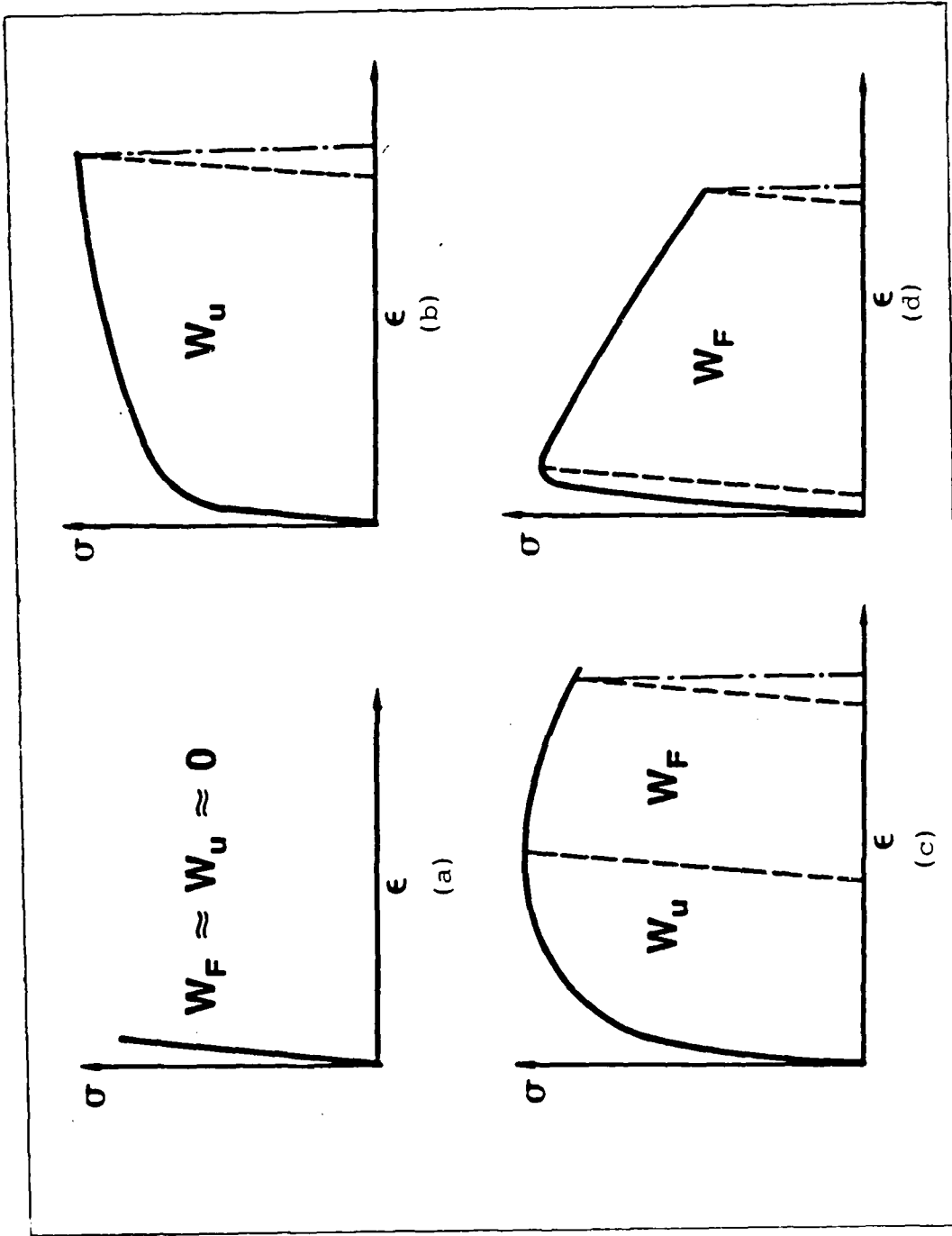


Figure 33. Relationship Between W_f and W_u for Different Stress-Strain Curves (6)

Recalling equation (10) for a finite width plate

$$W_u h_u = \frac{n}{n+1} \frac{\epsilon_{tpu} \sigma_{tu}}{Y^6} \left[1 - \left(\frac{\sigma_t}{\sigma_{tu}} \right)^{n+1} \right] h_f \frac{\epsilon_{tf} \epsilon_{tl}}{\epsilon_{tu} \epsilon_t} \left[\left(\frac{\epsilon_{tu}}{\epsilon_t} \right)^{\frac{n-1}{n}} - 1 \right] \phi \quad (10)$$

where

- n = the Ramberg-Osgood exponent for true plastic tensile strain
- σ_{tpu} = true plastic tensile strain at start of necking
- σ_{tu} = true ultimate tensile stress
- Y = geometric correction factor
- σ_t = true tensile stress
- h_f = effective height of slip band, .000557 in
- ϵ_{tf} = true tensile strain at $\sigma = \sigma_f$
- ϵ_{tu} = true tensile strain at start of necking
- ϵ_{tl} = true tensile strain at $\sigma = \sigma_l$
- ϵ_t = true tensile strain
- ϕ = thickness parameter

The modified Bockrath-Glassco method requires a rapid heating stress-strain curve (Figure 30) at the temperature of interest. The quantities that must be taken from the stress-strain curve are as follows:

- σ_u : ultimate tensile stress
- σ_y : yield stress
- σ_f : tensile stress at failure
- σ_{uf} : average tensile stress from 0.995 σ_u to σ_f
- ϵ_u : tensile strain at start of necking (0.995 σ_u)
- ϵ_f : tensile strain at failure
- E : Young's Modulus

Again, because of the shape of the stress-strain curves

$$\sigma_u = \sigma_y = \sigma_{uf}$$

and

$$\epsilon_u = \epsilon_f$$

Using the above values from the stress-strain curve, the

derived quantities necessary to solve equation (10) are computed as follows:

σ_{tu} is obtained by iteration using the following equation:

$$\sigma_{tu} = \frac{\sigma_u (1 + \epsilon_u)}{\left(1 - \frac{v\sigma_{tu}}{E}\right)^2} e^{(\sigma_{tu}/E)} \quad (23)$$

$$\epsilon_{tu} = \ln(1 + \epsilon_u) \quad (24)$$

$$\epsilon_{tpu} = \epsilon_{tu} - \sigma_{tu}/E \quad (25)$$

Next, σ_{ty} is also solved by iteration using

$$\sigma_{ty} = \frac{\sigma_y e^{(\epsilon_{tpy})}}{\left(1 - \frac{v\sigma_{ty}}{E}\right)^2} \quad (26)$$

where

$$\epsilon_{tpy} = \ln(1 + \epsilon_{ty}) = 0.001998 \text{ (0.2\% offset method for yield stress)} \quad (27)$$

The Ramberg-Osgood exponent, n , is found by

$$n = \frac{\ln\left(\frac{\epsilon_{tpu}}{\epsilon_{tpy}}\right)}{\ln\left(\frac{\sigma_{tu}}{\sigma_{ty}}\right)} \quad (28)$$

$$\epsilon_{pl} = 0.0005 \left[0.72 \left(\sigma_u / \sigma_y \right)^2 \right] \quad (29)$$

$$\sigma_{tl} = \sigma_{tu} \left[\epsilon_{pl} / \epsilon_{tpu} \right]^{1/n} \quad (30)$$

$$\epsilon_{tl} = \epsilon_{pl} + \sigma_{tl}/E \quad (31)$$

$$\epsilon_{tf} = \epsilon_{tu} \text{ (when } \epsilon_u = \epsilon_f \text{)} \quad (32)$$

$$Y = 1/[\sec(a\pi/W)]^{1/2} \quad (33)$$

$$\phi = 0.127 \quad (34)$$

Substituting (22) and (10) into (21) yields the equation for critical crack length as a function of stress for a given temperature.

$$a = \frac{E}{\pi\sigma^2\mu Y^2} \left(2T + \frac{n}{n-1} \frac{\epsilon_{tpu} \sigma_{tu}}{Y^6} \right) \quad (35)$$

$$\left[1 - \left(\frac{\sigma_t}{\sigma_{tu}} \right)^{n+1} \right] h \frac{\epsilon_{tf} \epsilon_{tl}}{\epsilon_t \epsilon_{tu}} \left[\left(\frac{\epsilon_{tu}}{\epsilon_t} \right)^{\frac{n-1}{n}} - 1 \right] \phi$$

where

$$\mu = (1 - \nu^2) \quad (36)$$

APPENDIX C: Critical Crack Length Calculations using Ductile Fracture Mechanics

Using the calculation procedure outlined in Appendix B with the rapid heating strength properties from MDAC (18), the critical crack length as a function of stress was computed. The calculations are for two failure temperatures, 150°C and 370°C, and for several plate widths. The tabulated values are plotted in Figures 31 and 32.

150°C (300°F)

Input Parameters (18): $\sigma_u = 38$ ksi $\epsilon_u = 0.16$
 $\sigma_y = 37.2$ ksi $\epsilon_f = 0.16$
 $\sigma_f = 38$ ksi $E = 11.1 \text{ E}+6$ psi
 $\sigma_{uf} = 38$ ksi

Calculated Parameters: $\sigma_{tu} = 44.01$ ksi $n = 26.06$
 $\sigma_{tf} = 44.01$ ksi $I = 6.25 \text{ E}-3$ lb/in
 $\sigma_{ty} = 37.35$ ksi

TABLE C.1

Critical Crack Length Versus Stress
 Using Ductile Fracture Mechanics
 at 150°C

W = Infinite		W = 10 in		W = 3 in	
a	σ	a	σ	a	σ
0.2	24.406	0.2	24.396	0.2	23.912
0.5	19.353	0.5	19.070	0.3	20.930
1.0	16.189	0.8	16.589	0.4	18.712
2.0	13.526	1.0	15.370	0.5	16.680
4.0	11.493	1.5	12.942	0.7	13.085
10.2	8.927	2.0	10.914	0.9	9.675
50.2	5.896	3.0	7.098	1.2	4.528
80.2	5.210	4.0	3.307	1.3	2.928
100.2	4.916				
170.2	4.269				

370°C (700°F)

Input Parameters (18): $\sigma_u = 14 \text{ ksi}$ $\epsilon_u = 0.16$
 $\sigma_y = 13.6 \text{ ksi}$ $\epsilon_f = 0.16$
 $\sigma_f = 14 \text{ ksi}$ $E = 0.722 \text{ E}+6 \text{ psi}$
 $\sigma_{uf} = 14 \text{ ksi}$

Calculated Parameters: $\sigma_{tu} = 16.22 \text{ ksi}$ $n = 24.79$
 $\sigma_{tf} = 16.22 \text{ ksi}$ $T = 4.07 \text{ E}-3 \text{ lb/in}$
 $\sigma_{ty} = 13.64 \text{ ksi}$

TABLE C.2

Critical Crack Length Versus Stress
 Using Ductile Fracture Mechanics
 at 370°C

W = Infinite		W = 10 in		W = 3 in	
a	σ	a	σ	a	σ
0.20	11.506	0.20	11.461	0.20	11.364
0.35	10.174	0.35	10.152	0.35	9.505
0.50	9.311	0.50	9.176	0.50	8.043
0.80	8.191	0.80	7.953	0.65	6.695
1.10	7.582	0.95	7.546	0.80	5.449
2.00	6.497	1.10	7.149	0.95	4.150
3.05	5.839	2.00	5.212	1.10	2.882
4.40	5.664	3.05	3.187		
25.10	3.316				
75.10	2.457				
150.10	2.027				

Appendix D: Data Tables

This section contains the test data from each of the tensile and fracture toughness tests conducted during the present study. The tensile test results are presented first followed by the fracture toughness tests.

TABLE D.1

Room Temperature Tensile Tests of 6061 T-6 Aluminum
(.061 in thick)

Date	Specimen	Width (in)	Area (in ²)	L_y (lb)	L_f (lb)	σ_y (ksi)	σ_u (ksi)
9/1	E4	1.5	.0915	-	4829.2	-	52.8
9/4	E5	1.5	.0915	-	4840.2	-	52.9
9/4	E6	1.5	.0915	-	4829.2	-	52.8
9/8	T2	1.0	.0610	2925	3121.1	48.0	51.2
9/8	T3	1.0	.0610	2950	3066.9	48.4	50.3
9/8	T4	1.0	.0610	2940	3050.0	48.2	50.0
9/8	E'1	1.18	.0736	-	3863.8	-	52.5
9/8	E'2	1.16	.0717	3450	3701.3	48.1	51.6
E (average) = 11.8 E+6 psi							

TABLE B.2

Room Temperature Tensile Tests of 6061 T-6 Aluminum
(.033 in thick)

Date	Specimen	Width (in)	Area (in ²)	L_y (lb)	L_f (lb)	σ_y (ksi)	σ_u (ksi)
9/1	F1	1.5	.0495	-	2313.9	-	46.7
9/4	F5	1.5	.0495	-	2279.5	-	46.1
9/4	F4	1.5	.0495	-	2280.9	-	46.1
9/4	F6	1.5	.0495	-	2237.7	-	45.2
9/8	F3	1.5	.0495	2000	2276.5	40.4	46.0
9/8	TT1	1.0	.0330	1260	1478.9	38.2	44.8
9/8	TT2	1.0	.0330	1260	1493.5	38.2	45.3

E (average) = 10.11 E+6 psi

TABLE D.3

Rapid Heating Tensile Tests of 6061 T-6 Aluminum
(1.5 in wide, .061 in thick)

Date	Specimen	I (W/cm ²)	t (sec)	T_f (C)	\dot{T} (C/sec)	L_f (lb)	σ_u (ksi)	σ/σ_{rt}
8/26	E1	996	0.283	344	1211	1740	19.0	.37
8/26	E2	996	2.57	358	139	1740	19.0	.37
8/26	E3	398	22.3	354	16	1740	19.0	.37

TABLE D.4

Room Temperature Fracture Toughness (K_C^*) and
 Net Section Limit Loads (P_1 , P_u) for 6061 T-6 Aluminum
 (.061 in thick)

Date	Specimen	Width	a	L_f	σ_u	K_C^*	P_1	P_u
		(in)	(in)	(lb)	(ksi)		(lbs)	(lbs)
Single Edge Notched Specimen								
6/19	A5	1.5	0.38	2665	29.1	48.2	2530	2720
9/4	A35	1.5	0.331	2917.5	31.9	46.3	2786	2994
9/4	A34	1.5	0.334	2917.5	31.9	46.7	2770	2977
9/4	A37	1.5	0.30	3154.1	34.7	46.0	2953	3174
Center Cracked Panels								
9/16	G5	1.5	0.3	2716.8	29.7	32.0	2646	2843
9/16	G6	1.5	0.3	2819.3	30.8	33.3	2645	2843
9/16	M1	1.0	0.3	1373.4	22.5	28.5	1176	1264

TABLE D.5

Room Temperature Fracture Toughness (K_C^*) and
 Net Section Limit Loads (P_1 , P_u) for 6061 T-6 Aluminum
 (.033 in thick)

Date	Specimen	Width	a	L_f	σ_y	K_C^*	P_1	P_u
		(in)	(in)	(lb)	(ksi)		(lbs)	(lbs)
Single Edge Notched Specimen								
6/19	B10	1.5	.325	1400	28.3	40.4	1224	1446
9/4	B36	1.5	.331	1456.2	29.4	42.7	1210	1429
9/4	B33	1.5	.331	1445.2	29.2	42.4	1210	1429
9/4	B11	1.5	.34	1385.1	28.0	41.6	1189	1405
9/4	B38	1.5	.30	1539.7	31.1	41.5	1283	1515
Center Cracked Panels								
9/4	H1	1.5	.15	1675.0	33.8	23.2	1533	1818
9/4	H2	1.5	.15	1644.4	33.2	22.8	1533	1810
9/16	H5	1.5	.30	1291.4	26.1	28.2	1150	1357
9/16	N1	1.0	.30	639.5	19.4	24.5	511	603

TABLE D.6

Rapid Heating Rate Fracture Toughness (K_C^*) and
 Net Section Limit Load (P_1) for 6061 T-6 Aluminum
 (1.5 in wide, .061 in thick)

Date	Specimen	l	t	a	L_i	L_f	\dot{T}	T_f	K_C^*	P_1
		(W/cm ²)	(s)	(in)	(lbs)	(lbs)	(C/s)	(°C)		(lbs)
SEN										
7/24	A27	.4	15.48	.370	1740	1740	20	308	30.6	1401
7/23	A31	.4	10.40	.370	2260	2260	20	211	39.8	2182
7/23	A29	.2	16.25	.394	800	800	23	367	15.0	885
7/24	A28	.4	9.96	.370	1740	1740	29	285	30.6	1638
7/22	A21	1.0	4.23	.363	800	800	95	403	13.8	733
7/22	A22	1.0	1.87	.343	2260	2260	103	192	37.0	2341
7/21	A40	1.0	2.45	.394	1740	1740	113	277	32.6	1623
7/22	A23	1.0	2.70	.347	800	800	148	398	13.3	756
7/22	A26	1.0	1.71	.448	1740	1740	163	279	37.4	1403
7/23	A2	1.0	0.33	.363	800	740	1169	386	12.8	812
7/23	A25	1.0	0.14	.363	2260	2260	1215	175	37.0	2311
8/26	A6	1.0	0.29	.320	800	710	1162	362	11.3	1053
8/26	A33	1.0	0.19	.331	2260	2170	1153	242	35.5	2090
7/23	A24	1.0	0.23	.355	1200	1230	1392	313	20.8	1396
7/23	A30	1.0	0.15	.413	1740	1680	1497	229	33.1	1860
CCP										
8/25	G2	0.9	4.16	.173	2260	2260	68	292	18.4	2113
8/26	G3	1.0	7.0	.181	900	900	58	417	7.3	770
8/26	G1	1.0	0.25	.181	2260	2204	1284	329	18.3	1540
8/26	G4	1.0	0.34	.173	900	900	1174	405	7.8	770

AD-A169 745

THE EFFECTIVE FRACTURE TOUGHNESS OF ALUMINUM AT RAPID
HEATING RATES(U) AIR FORCE INST OF TECH
WRIGHT-PATTERSON AFB OH SCHOOL OF ENGINEERING

2/2

UNCLASSIFIED

J W NICHOLS DEC 87 AFIT/GAE/AA/87D-14

F/G 11/6.1

NL



1-C
1-1
1-25
1-4
1-6
2-8
2-2
2-0
1-8
3-15
3-5
4-0
4-5

TABLE D.7

Rapid Heating Rate Fracture Toughness (K_C^*) and
 Net Section Limit Load (P_1) for 6061 T-6 Aluminum
 (1.5 in wide, .033 in thick)

Date	Specimen	I	t	a	L_i	L_f	\dot{T}	T_f	K_C^*	P_1
		(W/cm ²)	(s)	(in)	(lbs)	(lbs)	(C/s)	(C)		(lbs)
SEN										
7/23	B30	.4	21.16	.339	500	500	17	362	15.0	453
7/24	B29	.4	21.80	.355	400	400	18	398	12.5	323
7/24	B16	.4	12.53	.316	940	940	19	244	26.5	921
7/24	B28	.4	3.60	.320	1220	1220	43	157	34.7	1125
7/23	B22	.4	4.43	.327	1220	1220	44	195	35.4	1037
7/22	B21	1.0	5.38	.320	400	130	84	450	3.7	247
8/25	B3	0.9	4.40	.30	400	400	91	402	10.8	359
7/23	B30	1.0	3.90	.339	500	500	99	386	15.0	358
7/22	B26	1.0	3.90	.323	600	450	102	398	12.9	344
7/21	B23	1.0	1.70	.331	1220	1220	135	229	35.8	944
7/21	B24	1.0	1.50	.347	940	940	142	213	28.8	950
7/22	B8	1.0	0.10	.32	940	771	1565	157	22.0	1125
7/23	B19	1.0	0.19	.32	500	380	1792	340	10.8	530
7/23	B2	1.0	0.13	.331	940	800	1833	229	23.5	944
8/26	B27	1.0	0.20	.316	400	400	1847	375	11.3	448
8/25	B13	1.0	0.11	.315	1220	1040	1886	198	29.2	1048
7/23	B12	1.0	0.10	.319	1220	1010	2291	229	28.7	966
8/26	B32	1.0	0.11	.331	800	650	2864	315	19.1	617
CCP										
8/26	H3	1.0	0.75	.228	1220	1220	200	156	35.4	1200
8/26	H4	1.0	0.11	.244	1220	1010	2090	237	19.1	1008

Bibliography

1. "A Compilation of Fracture and Crack Growth Data for High-Strength Alloys," Damage Tolerant Design Handbook, Volume 3, compiled by J. Gallagher. Columbus OH: Battelle, 1983.
2. Adachi, J. and others. Laser Produced Strength Degradation of Plates in Tension and Tubes in Torsion. AMMRC-IR-78-17. Army Materials Technology Laboratory, Watertown MA, April 1978.
3. Aerospace Structural Metals Handbook, Volume 3, edited by J. Wolf. Traverse City MI: Mechanical Properties Data Center, 1973.
4. Bagford, John. Drawings of LHMEI floor plan and equipment. Accurex Corp, Dayton OH, August 1987.
5. Bockrath, G. E. and J. B. Glassco. Fracture Mechanics of Ductile Metals. Company Report. McDonnell Douglas Astronautics Company, Huntington Beach CA, 1974, revised 1985.
6. Bozich, W. F. and others. "Liquid Propellant Ballistic Missile Vulnerability Program," LHX-1 Review Meeting. Air Force Weapons Laboratory, Kirtland AFB NM, 22-23 October, 1985.
7. Broek, David. Elementary Engineering Fracture Mechanics (Fourth Revised Edition). Dordrecht, The Netherlands: Martinus Nijhoff Publishers, 1986.
8. Department of Defense. MIL Handbook 5-D. Washington: Government Printing Office, 1 June 1983.
9. Dornheim, Michail A. "Missile Destroyed in First SDI Test at High Energy Laser Facility," Aviation Week and Space Technology, September 23, 1985.
10. Farahmand, B. and W. F. Bozich. Crack Initiation and Propagation in Ductile Metals at Elevated Temperature. Company Report. McDonnell Douglas Astronautics Company, Huntington Beach CA, 1986.
11. Gagliano, F. P. and U. J. Zalekas. Lasers in Industry, edited by S. S. Charschan. New York: Van Nostrand Reinhold Company, 1972.
12. Garofalo, Frank. Fundamentals of Creep and Creep-Rupture in Metals (Second Printing). New York: The Macmillan Company, 1966.

13. Holman, James P. Experimental Methods for Engineers (Second Edition). New York: McGraw Hill Book Company, 1978.
14. Kanninen, Melvin F. and Carl H. Popelar. Advanced Fracture Mechanics. New York: Oxford University Press, 1985.
15. Licata, Raymond J. Beam Profiling of a Multimode Laser. MS Thesis, AFIT/GEP/PH/78D-7. School of Engineering, Air Force Institute of Technology (AU), Wright-Patterson AFB OH, December 1978.
16. Mohr, Charles. "Success Reported in Test of Laser," The New York Times, September 13, 1985.
17. Omega 86 Temperature. Product Catalog. Omega Engineering Inc, Stamford CT, 1986.
18. Straw, A. D. "Ductile Fracture Computations for 6061 T-6 Aluminum at Elevated Temperatures." Telephone Facsimile. McDonnell Douglas Astronautics Company, Huntington Beach CA, November 3, 1987
19. Tetelman, A. S. and A. J. McEvily, Jr. Fracture of Structural Materials. New York: John Wiley & Sons, Inc, 1967.
20. Torvik, Peter J. On the Generation of Stress and Deformation in Elastic Solids By High Powered Lasers. AFIT IR 80-6. Air Force Institute of Technology (AU), Wright-Patterson AFB OH, September 1980.
21. ----. Thermal Response Calculations and their Role in the Design of Experiments. AFIT IR 73-6. Air Force Institute of Technology (AU), Wright-Patterson AFB OH, December 1973.
22. Wenzel, Richard. "Standardized Material Properties for Selected Metals," Personal Communication. Naval Research Laboratory, Washington DC, 1985.
23. Witzell, W. E. and N. R. Adsit. "Temperature Effects on Fracture," Fracture, Volume IV, edited by H. Liebowitz. New York: Academic Press, 1969.

Uita

Captain Joseph W. Nichols was born on 13 Nov 1959 in Wichita, Kansas. He graduated from Gwynn Park High School in Brandywine, Maryland, in 1977. Next, he attended Brigham Young University in Provo, Utah, from which he received the degree of Bachelor of Science in Mechanical Engineering in 1983. After graduation, he was commissioned in the USAF and was assigned to the Air Force Weapons Laboratory at Kirtland AFB, New Mexico. There he conducted research into the effects of laser radiation on aerospace materials and structures and authored several papers based upon the results of this work. In June 1986, he entered the School of Engineering, Air Force Institute of Technology.

Permanent Address: 6101 E. Calle Tuberia
Scottsdale, AZ 85251

UNCLASSIFIED

SECURITY CLASSIFICATION OF THIS PAGE

0189 945

REPORT DOCUMENTATION PAGE

Form Approved
OMB No. 0704-0188

REPORT SECURITY CLASSIFICATION UNCLASSIFIED		1b. RESTRICTIVE MARKINGS	
2a. SECURITY CLASSIFICATION AUTHORITY		3. DISTRIBUTION / AVAILABILITY OF REPORT Approved for public release; distribution unlimited.	
2b. DECLASSIFICATION / DOWNGRADING SCHEDULE			
4. PERFORMING ORGANIZATION REPORT NUMBER(S) AFIT/GAE/AA/87D-14		5. MONITORING ORGANIZATION REPORT NUMBER(S)	
6a. NAME OF PERFORMING ORGANIZATION School of Engineering	6b. OFFICE SYMBOL (if applicable) AFIT/ENY	7a. NAME OF MONITORING ORGANIZATION	
6c. ADDRESS (City, State, and ZIP Code) Air Force Institute of Technology Wright-Patterson AFB OH 45433-6583		7b. ADDRESS (City, State, and ZIP Code)	
8a. NAME OF FUNDING / SPONSORING ORGANIZATION Air Force Weapons Lab	8b. OFFICE SYMBOL (if applicable) AFWL/TA	9. PROCUREMENT INSTRUMENT IDENTIFICATION NUMBER	
8c. ADDRESS (City, State, and ZIP Code) Air Force Weapons Laboratory Kirtland AFB NM 87117-6008		10. SOURCE OF FUNDING NUMBERS	
		PROGRAM ELEMENT NO.	PROJECT NO.
		TASK NO.	WORK UNIT ACCESSION NO.
11. TITLE (Include Security Classification) See Box 19			
PERSONAL AUTHOR(S) Joseph W. Nichols, Capt, USAF			
13a. TYPE OF REPORT MS Thesis	13b. TIME COVERED FROM _____ TO _____	14. DATE OF REPORT (Year, Month, Day) December 1987	15. PAGE COUNT 99
16. SUPPLEMENTARY NOTATION			
17. COSATI CODES		18. SUBJECT TERMS (Continue on reverse if necessary and identify by block number)	
FIELD	GROUP	Fracture Toughness, Temperature Effects, Rapid Heating, Laser Effects, Mechanical Properties (A1)	
20	11		
17	05		
19. ABSTRACT (Continue on reverse if necessary and identify by block number)			
11. Title: The Effective Fracture Toughness of Aluminum at Rapid Heating Rates			
Thesis Advisor: Dr Shankar Mall Associate Professor of Mechanics			
ABSTRACT ON BACK			
20. DISTRIBUTION / AVAILABILITY OF ABSTRACT <input checked="" type="checkbox"/> UNCLASSIFIED/UNLIMITED <input type="checkbox"/> SAME AS RPT. <input type="checkbox"/> DTIC USERS		21. ABSTRACT SECURITY CLASSIFICATION	
22a. NAME OF RESPONSIBLE INDIVIDUAL Dr S. Mall		22b. TELEPHONE (Include Area Code) (513) 255 3517	22c. OFFICE SYMBOL AFIT/ENY

Approved for public release: IAW AFR 190-1.
 E. WOLAW 22 Feb 88
 Director for Research and Professional Development
 Air Force Research Laboratory (AFRL)
 Wright-Patterson Air Force Base

UNCLASSIFIED

19. Abstract:

The fracture of aluminum plates, at high temperatures and at rapid heating rates, was investigated using 6061 T-6 aluminum as the test material. Three heating rates were tried—low ($15^{\circ}\text{C}/\text{sec}$), medium ($150^{\circ}\text{C}/\text{sec}$), and high ($1500^{\circ}\text{C}/\text{sec}$).

Rapid heating and room temperature tensile tests were performed to characterize the material as a function of temperature. Single edge notched specimen and center cracked panels were fabricated for use in fracture tests. A modified linear elastic fracture toughness, called the effective fracture toughness, or K_{IC}^* was used to quantify the relationship between fracture toughness and temperature. The K_{IC}^* was found to decrease as temperature increased in the same manner as the strength. Heating rate, at least in the range tested, had little effect on either the strength or the fracture toughness. Further, it was found that the fracture behavior of 6061 T-6 aluminum under the tested conditions can be related to net-section yielding.

A ductile Fracture model was found to be useful in relating the critical crack size to critical stress. The test data from the present study showed good agreement with this model.

(Keynote paper)

UNCLASSIFIED

END

DATE

FILMED

APRIL

1988

DTIC